6-12-2020

Measuring Channel Planform Change From Image Time Series: A Generalizable, Spatially Distributed, Probabilistic Method for Quantifying Uncertainty

Christina M. Leonard
Utah State University, christina.leonard@aggiemail.usu.edu

Carl J. Legleiter
U.S. Geological Survey

Devin M. Lea
University of Oregon

John C. Schmidt
Utah State University, jack.schmidt@usu.edu

Recommended Citation

Leonard, C. M., Legleiter, C. J., Lea, D. M., and Schmidt, J. C. (2020) Measuring channel planform change from image time series: A generalizable, spatially distributed, probabilistic method for quantifying uncertainty. Earth Surf. Process. Landforms, https://doi.org/10.1002/esp.4926.

Measuring channel planform change from image time series: A generalizable, spatially distributed, probabilistic method for quantifying uncertainty

Revised manuscript submitted to Earth Surface Processes and Landforms

Christina M. Leonard[1], Carl J. Legleiter[2], Devin M. Lea[3], John C. Schmidt[1]

[1] Department of Watershed Sciences, Utah State University, 5210 Old Main Hill, Logan, UT 84322-5210

[2]U.S. Geological Survey, Integrated Modeling and Prediction Division, Golden, CO 80403

[3] Department of Geography, University of Oregon, 1251 University of Oregon, Eugene, OR 97403-1251

*corresponding author *christina.leonard@aggiemail.usu.edu*

Key words: channel change, remote sensing, change detection uncertainty, probabilistic, fluvial geomorphology

Abstract

Channels change in response to natural or anthropogenic fluctuations in streamflow and/or sediment supply and measurements of channel change are critical to many river management applications. Whereas repeated field surveys are costly and time consuming, remote sensing can be used to detect channel change at multiple temporal and spatial scales. Repeat images have been widely used to measure long-term channel change, but these measurements are only significant if the magnitude of change exceeds the uncertainty. Existing methods for characterizing uncertainty have two important limitations. First, while the use of a spatially variable image co-registration error avoids the assumption that errors are spatially uniform, this type of error, as originally formulated, can only be applied to linear channel adjustments, which provide less information on channel change than polygons of erosion and deposition. Second, previous methods use a level-of-detection (LoD) threshold to remove non-significant measurements, which is problematic because real changes that occurred but were smaller than the LoD threshold would be removed. In this study, we present a new method of quantifying uncertainty associated with channel change based on probabilistic, spatially varying estimates of co-registration error and digitization uncertainty that obviates a LoD threshold. The spatially distributed probabilistic (SDP) method can be applied to both linear channel adjustments and polygons of erosion and deposition, making this the first uncertainty method generalizable to all metrics of channel change. Using a case study from the Yampa River, Colorado, we show that the SDP method reduced the magnitude of uncertainty and enabled us to detect smaller channel changes as significant. Additionally, the distributional information provided by the SDP method allowed us to report the magnitude of channel change with an appropriate level of confidence in cases where a simple LoD approach yielded an indeterminate result.

1. Introduction

Despite recent advancements in remote sensing platforms, historic aerial images remain invaluable in the analysis of long-term channel change. These data are windows into the past, providing a rich, spatially robust history of channel change during the ~100 years since the first air photos were taken (Rhoades et al., 2009; Comiti et al., 2011; Bollati et al., 2014). Programs like Google Earth are a powerful means to visualize channel evolution, because a sequence of aerial images can be easily compared. Although such programs facilitate the casual inspection of channel evolution, they cannot be used to make the precise measurements of channel change that are required for most management applications. Additionally, the aerial and/or satellite images available in these programs only date to the mid-1990s and thus provide only a limited window to the past. Thus, programs like Google Earth cannot entirely replace detailed analyses of channel change that involve geo-referencing and overlaying historic aerial images to quantify changes in channel location over time.

Predicting channel change is a longstanding problem in the field of geomorphology. Since the mid-20th century, water resource development and climate change have significantly altered the flow and sediment supplied to most of the world's rivers (Nilsson et al., 2005; Schmidt and Wilcock, 2008; Best, 2019), creating a societal need to understand how such disturbances affect flood risk, ecosystem management and rehabilitation, and land use planning. Case studies of channel change – how much, at what rate, and why – are the primary means of understanding the trajectory of channel adjustment after a disturbance. In many cases repeat aerial images are the only record of the pre-disturbed channel and thus provide the most complete record of the channel's response. Therefore, studies of channel change using historic aerial images remain of fundamental interest to geomorphologists and those tasked with effectively managing river systems.

Channel change measured from aerial images is only significant if the magnitude of bank erosion or floodplain formation exceeds the magnitude of uncertainty in the channel change analysis (Downward et al., 1994). The existing body of channel change literature includes numerous case studies that use a wide range of methods, which vary in rigor and complexity, to quantify this uncertainty. As a result and for a given case study, one might conclude that the channel changes identified are, or are not, significant depending on how the uncertainty of that analysis is quantified. The simplest methods assume that the magnitude of uncertainty is negligible compared to the magnitude of channel change and can be disregarded (e.g., Lyons et al., 1992; Merritt and Cooper, 2000; Buckingham and Whitney, 2007; Magilligan et al., 2008; Cadol et al., 2011; Comiti et al., 2011; Schook et al., 2017; Wellmeyer et al., 2005), or assume that the uncertainties compensate for one another in the calculation of net channel change and can be disregarded (Gaeuman et al., 2003; Ham and Church, 2000). A more complex approach to quantifying uncertainty is to establish a level-of-detection (LoD); measurements of channel change that are smaller in magnitude than this threshold cannot be distinguished from uncertainty and are removed from the analysis (Urban and Rhoads, 2003). In most studies, the LoD is specified as a spatially uniform threshold for designating measurements as non-significant and excludes these measurements from the analysis (Winterbottom and Gilvear, 2000; White et al., 2010; Martin and Pavlowsky, 2011; Kessler et al., 2013). This approach causes a large number of small planform changes to be removed from the analysis and introduces a bias by ignoring polygons of very small channel change, implying that the reach-scale average will be dominated by polygons of larger channel change. Lea and Legleiter (2016) partially overcame this limitation by allowing the LoD to vary spatially based on local estimates of image co-registration error, which resulted in a larger proportion of measurements being retained as statistically significant and thus improved the ability to detect actual channel change.

Despite an abundance of methods used to quantify the uncertainty in measurements of channel change from aerial images, a generalizable, robust methodology is lacking. Several metrics are used to measure channel change from repeat aerial images, and previous methods to quantify uncertainty have varied depending on the metric of channel change used in individual case studies. This situation has hindered the development of a generalizable uncertainty method and makes comparing case studies of channel change from image time series more difficult and imprecise than studies of repeat topography, for which generalizable methods for characterizing uncertainty have been developed (Brasington et al., 2003; Wheaton et al., 2010). For example, although the method developed by Lea and Legleiter (2016) (hereafter referred to as the spatially variable registration error (SVRE) method) was a significant improvement upon spatially uniform methods of quantifying image co-registration error, this method can only be applied to linear channel adjustments, such as comparison of channel centerlines for measuring rates of meander migration (Nanson and Hickin, 1983; Micheli and Kirchner, 2002; Schook et al., 2017; Donovan and Belmont, 2019) or bank lines for measuring rates of bank retreat (Urban and Rhoads, 2003; De Rose and Basher, 2011; Day et al., 2013; Kessler et al., 2013). An alternative to this simplified linear representation of channel form involves analyzing the area of bank erosion and/or floodplain formation by delineating polygons of erosion and deposition (Gaeuman et al., 2003; Grams and Schmidt, 2005; White et al., 2010; Swanson et al., 2011; Nelson et al., 2013; Nardi and Rinaldi, 2015). Polygons of erosion and deposition are often a more informative measure of channel change, because these polygons can be used to characterize fundamental attributes of channels (e.g., lateral channel stability) and evaluate the processes by which channels change size. An uncertainty method that allows for spatially varying image co-registration error and can be applied to both linear and areal metrics of channel change thus would be useful.

Another significant limitation of the SVRE and other uncertainty methods is the removal of any channel change measurements smaller than a specific threshold. This LoD approach is problematic, because measured changes less than the specified threshold are assumed to not represent real change and are removed from the analysis. However, including as many measurements of channel change as possible, whether small or large, is important, because those data contribute to our understanding of the processes and mechanisms by which channels adjust. Additionally, the cumulative effect of many small measurements of change might be larger than the effect of a few measurements of large change; thus, excluding small measurements might give the false impression that the channel’s response is to adjust in a few areas dominated by large change. Also, preferentially removing small changes could lead to biased removal of erosional areas, because erosion tends to be more spatially focused than deposition (Brasington et al., 2003). Similar concerns with the LoD threshold also exist when estimating volumes of erosion and deposition from two topographic surfaces

(Brasington et al., 2003; Anderson and Pitlick, 2014; Leonard et al., 2017; Anderson, 2019). In this case, the LoD threshold tends to preferentially remove polygons of deposition, because deposition occurs as relatively thin deposits over large areas (e.g., bars) whereas polygons of erosion are typically localized and thick (Brasington et al., 2003). In some instances, the biased removal of deposition can cause the true value of volumetric change to fall outside the 95% confidence interval of the volumetric change obtained by removing measurements below the LoD threshold (Anderson, 2019).

In this study, we introduce a generalizable method for quantifying the uncertainty associated with measurements of channel change from repeat aerial images based on spatially varying estimates of uncertainty; we call this the Spatially Distributed Probabilistic (SDP) method. The SDP method can be applied to all metrics of channel change calculated from the comparison of repeat aerial images, making this technique the first robust, generalizable method for quantifying uncertainty in measurements of channel change from an image time series. Moreover, the SDP approach provides a probability distribution of planform change as output, rather than a single value with an associated uncertainty, and thus allows the user to estimate the probability that net change was erosional, depositional, or within a specified tolerance of a net sediment balance (i.e., zero net flux).

2. Spatially distributed probabilistic (SDP) method of quantifying the uncertainty associated with change detection from an image time series

The purpose of this section is to provide a general overview of the SDP method. Step-by-step instructions for implementing the method can be found in the supplemental information, and both a standalone application and the corresponding MATLAB® source code for performing an SDP uncertainty analysis are available at https://qcnr.usu.edu/coloradoriver/files/leonard_data.

The SDP method considers one source of error - image co-registration - and two sources of uncertainty - digitization and interpretation - in measurements of channel change from repeat aerial images. We define a source of error as having a deviation from a known value and a source of uncertainty as having a range of values that encompass the true measurement. Unlike previous methods that consider multiple sources of error and uncertainty in channel change analysis, the SDP method does not use error propagation to derive a single value to summarize the uncertainty. Instead, each source of error and uncertainty is used to create a probabilistic delineation of the active channel boundary for each of the two images from which a distribution of channel change measurements can be derived.

2.1. Image co-registration error

Image co-registration error is related to misalignment in image overlays that can mask real channel change or give a false impression of change when none has occurred (Gaeuman et al., 2005). Image misalignment originates from the need to transform the original row, column pixel coordinates of each digital image to a real-world coordinate system (e.g., a Universal Transverse Mercator (UTM) projection). This process is referred to as image warping and involves finding pairs of identifiable features on an image whose pixel coordinates are in a row, column, or arbitrary local system, referred to as the warp image, and an image that already has been geo-referenced to the desired real-world coordinate system, referred to as the base image. These pairs of points are termed tie-points and are used to establish a spatial transformation that relates pixel coordinates in the warp image to map coordinates in the base image.

The SDP method uses a spatially distributed image co-registration error that is similar to that of the SVRE method, but we use independent test-points as recommended by Hughes et al. (2006) instead of using tie-points to generate the error surface. Test-points are identified by extracting the map coordinate of the same feature on the image that is being digitized and the most recent image in the time series (Figure 1; step 1a). Test-points differ from tie-points in that test-points are extracted from two images that are geo-referenced to a common coordinate system, and thus directly measure image overlay error rather than the residual error in the transformation used for image warping. Test-points also can be used to quantify co-registration error in images that are already geo-referenced and thus do not require warping, such as data acquired through the National Agriculture Imagery Program (NAIP) or from various satellite platforms. The magnitude of each test-point error is calculated in the X and Y directions by subtracting the test-point coordinate in the image being used to delineate the channel boundary (x_i', y_i') from the same test-point coordinate in the most recent image (x_i, y_i) (Figure 1 step 1b; Figure 2 a,b;):

$$\varepsilon_{xi} = x_i - x_i' ; \#(1)$$

$$\varepsilon_{yi} = y_i - y_i' ;\#(2)$$

where ε_{xi} is the magnitude of co-registration error in the X direction for the i^{th} test-point and ε_{yi} is the magnitude of co-registration error in the Y direction for the i^{th} test-point. A continuous surface of ε_x and ε_y is then created by triangulating between each ε_{xi} and ε_{yi}

point and using bi-linear interpolation within each triangle (Amidror, 2002; Figure 2 a,b). The triangulation is dependent on the spatial distribution of the test-points, however, and we account for this dependency by repeatedly withholding 10% of the test–points using a 10-fold cross-validation to generate 10 ε_x and ε_y surfaces (Figure 1 step 1c-e).

2.2. *Interpretation uncertainty*

Uncertainty in deciphering whether an alluvial surface is part of the active channel or part of the floodplain was originally discussed by Winterbottom and Gilvear (1997), but this aspect of uncertainty is rarely included in studies of channel change. Common indicators used to classify a surface as channel or floodplain include breaks in slope or the elevation of the surface relative to the surrounding floodplain. Such topographic features can only be identified in aerial images when viewed in stereo, but most studies of channel change delineate channel boundaries based on single images (i.e., not stereo pairs) examined within a geographic information system (GIS) software environment. Therefore, the location of the channel boundary is often inferred on the basis of vegetation density (Dean and Schmidt, 2011; Nelson et al., 2013) rather than topographic changes at the edge of the active channel. These delineations thus are subject to greater uncertainty than if image pairs were analyzed in stereo. Using vegetation density as a threshold for defining the edge of the channel is also problematic, because fast-growing perennial vegetation can encroach upon low elevation bars that are regularly inundated during the annual flood but exposed for long periods during base flow.

The SDP method explicitly incorporates the uncertainty inherent to interpreting the edge of the channel by delineating minimum and maximum active channel boundaries (Figure 1 step 2); Dean and Schmidt (2011, 2013) used a similar approach. We define the maximum active channel boundary (A_{max}) as the smallest extent of the vegetated islands and the largest extent of the active channel and the minimum active channel boundary (A_{min}) as the largest extent of the vegetated islands and the smallest extent of the active channel (Figure 3). Thus, A_{max} represents the maximum area of the active channel whereas A_{min} represents the minimum area of the active channel.

2.3. Digitization uncertainty

Uncertainty in digitizing the edge of the channel is the accuracy with which the same operator can repeatedly delineate the same boundary (Gurnell et al., 1994; Micheli and Kirchner, 2002; Donovan et al., 2019) and previously has been quantified using a single value, such as half the product of the width of a pencil line and the scale of the aerial image (Ham and Church, 2000; Gaeuman et al., 2003; Nelson et al., 2013). When digitizing the channel extent on an aerial image, the digitizing uncertainty is not uniform throughout the image and we account for this variability in the SDP method by characterizing the uncertainty probabilistically using a normal distribution with a mean of zero and a standard deviation assumed to be one-third of the maximum digitizing uncertainty. The maximum digitizing uncertainty can be estimated on a case-by-case basis by repeatedly delineating the same boundary or using the image scale and pencil width. Alternatively, the maximum digitizing uncertainty can be assumed to be similar to that of previous studies and taken to be a constant value, such as 2 m (e.g., Legleiter, 2014; Lea and Legleiter, 2016; Donovan et al, 2019).

2.4. Implementation of the SDP method

The SDP method creates a probabilistic delineation of the active channel boundary using information on all three sources of error and uncertainty described above: image co-registration, interpretation, and digitization. First, the method adjusts the A_{max} and A_{min} boundaries based on the local co-registration error by moving each vertex (x_j, y_j) along a vector whose magnitude $\left(\left\|\overrightarrow{\varepsilon_{xy}}\right\|\right)$ and direction (θ) (Figure 2c) are given by:

$$\left\|\overrightarrow{\varepsilon_{xy}}\right\| = \left(\varepsilon_{xj}{}^{2} + \varepsilon_{yj}{}^{2}\right)^{0.5};\#(3)$$

$$\theta = tan^{-1}\left(\frac{\varepsilon_{yj}}{\varepsilon_{xj}}\right);\#(4)$$

where ε_{xj} and ε_{yj} are the co-registration errors at point (x_j, y_j) extracted from the ε_x and ε_y surfaces (Figure 4a). This procedure is repeated for each of the 10 co-registration error surfaces to create 10 A_{max} and A_{min} boundaries (Figure 1 step 3). Along each of the 10 A_{max} and A_{min} boundaries, a band of delineations that represents digitizing uncertainty is generated by randomly sampling 100 digitization uncertainty values from the normal distribution and moving each vertex along a normal vector by the magnitude of the sampled uncertainty value (Figure 1 step 4; Figure 4b). The final probabilistic delineation for each A_{max} and A_{min} boundary consists of 1,000 delineations whose distribution represents co-registration and digitization uncertainty (Figure 4c).

After the probabilistic delineations for A_{max} and A_{min} boundaries are created for two aerial images (Figure 1 step 5), probability distributions of channel change are calculated by randomly sampling, with replacement, 5,000 A_{max} or A_{min} delineations from both aerial images and overlaying each sampled boundary to create polygons of erosion and deposition (Figure 1 step 6). This step is performed separately for each combination of A_{max} and A_{min} overlays, creating a total of 20,000 calculations of channel change (Figure 1 steps 7a-d): (a) minimum active channel boundary in both images ($A_{Min(t1)}$&$A_{Min(t2)}$); where the subscripts *t1* and *t2* denote the earlier and later images, respectively; (b) maximum active channel boundary in both images ($A_{Max(t1)}$&$A_{Max(t2)}$); (c) minimum active channel boundary in the earlier image and maximum active channel boundary in the later image ($A_{Min(t1)}$&$A_{Max(t2)}$); and (d) maximum active channel boundary in the earlier image and minimum active channel boundary in the later image ($A_{Max(t1)}$&$A_{Min(t2)}$). The distribution of areal changes for all combinations of overlays represents the combined uncertainty in co-registration, digitization, and interpretation.

The same method can be used to create a probabilistic delineation of channel centerlines or bank lines to obtain a distribution of centerline migration or bank retreat rates. Here, we focus on applying the SDP method to polygons of erosion and deposition because, as discussed in section 1, these measurements yield more geomorphic information.

3. Channel change case study

To illustrate how the SDP method can be applied in a specific channel change analysis, we describe application of the SDP method to a 23-km alluvial segment of the Yampa and Little Snake Rivers in northwestern Colorado, USA. Here, we describe our analysis of channel change based on analysis of aerial images collected in 1954 and 1961 (Figure 5). We demonstrate the advantages of the SDP method by comparing our results to those obtained using two methods that do not use a spatially variable image co-registration error and do not characterize uncertainty in a probabilistic manner. The data used in this case study are available from the U.S. Geological Survey (USGS) ScienceBase (Legleiter and Leonard, 2020). Both historical images were collected from late August to early September at base flow (i.e., 7.16 and 9.03 m^3s^{-1} in 1954 and 1961, respectively, estimated at the Deerlodge gage by summing the discharge at the Maybell (USGS station number: 09251000) and Lily (USGS station number: 09260000) gages); Figure 5). The flow regimes of the Yampa and Little Snake Rivers are largely unregulated and dominated by spring snowmelt floods. The mean annual flood at the Deerlodge gage is 408 m^3s^{-1}, and late summer is a time of low discharge (Manners et al., 2014; Topping et al., 2018). Both rivers in the study area have wide active channels with many active bars, as well as bars adjacent to the channel that were formed by floods of different magnitudes. The Little Snake River is the primary source of fine sediment to the Yampa River in Yampa Canyon in Dinosaur National Monument (Topping et al., 2018) and provides a disproportionately large supply of fine sediment relative to the river's contribution of streamflow (Andrews, 1980). We selected this location for our channel change case study, because the National Park Service is concerned about the maintenance of valued park resources that might be affected by upstream water development and recognizes the need to distinguish natural patterns of channel change from changes associated with anthropogenic perturbations.

3.1. Channel change case study methods

The 1954 and 1961 images were not geo-referenced to a projected coordinate system, so we warped both images to a common projected coordinate system using the 2017 NAIP image as a base. The 1954 and 1961 images were downloaded from the USGS Earth Explorer website (USGS, 2019) as 24 single frame images. In Section 2, we described the general process of image warping whereby tie-points are identified on an individual single frame image to develop a transformation equation for warping that particular image. In this case study, however, we used a Structure-from-Motion (SfM) software package (Agisoft LLC, 2016) to first align and merge the single frame images into a mosaic and then warp and rectify the mosaic by using 12 tie-points with elevations extracted from the National Elevation Dataset (USGS, 2012) to define a 7-parameter similarity transformation with three parameters for translation, three for rotation, and one for scaling. Other studies have demonstrated the utility of using SfM to reconstruct elevation models of landforms from historic aerial images (Riquelme et al., 2019), and we found that the same method was useful for geo-referencing a large number of historic aerial images; however, difficulties may arise when the overlap between adjoining images is small. Also, we avoided the misalignments that can occur at the seams of the images when they are individually geo-referenced and overlaid by using SfM to geo-reference the mosaic rather than the individual images (e.g., Donovan et al., 2019).

As described in Section 2, we used independent test-points to characterize co-registration error in our case study. These test-points indicated how well the 1954 and 1961 images overlaid on the 2017 NAIP image. In our case study, test-points were difficult to visually identify, because roads and buildings in the 2017 image were not present in the 1954 and 1961 images and “soft” tie-points were limited. Therefore, we used an area-based matching algorithm in the remote sensing software package ENVI® (L3Harris Geospatial) to automatically generate test-points (Figure 2a). The area-based matching algorithm compared grayscale values of each image within a moving search window and identified similarities and patterns using normalized cross-correlation. We removed test-points with correlation coefficients of less than 0.8, and we manually inspected the remaining test-points with the lowest correlation coefficients to ensure test-point accuracy. The algorithm produced approximately 450 test-points in both images, but the points were predominantly located on adjacent hillslopes with high textural variability, because the landscape in our case study was rural with high topographic variability. Therefore, we supplemented the ENVI-generated test-points with manually selected points along the valley bottom.

We used the methodology described in Section 2 to create spatially distributed ε_x and ε_y surfaces from the test-points generated above and calculate $\|\overrightarrow{\varepsilon_{xy}}\|$ and θ at any x_j, y_j point (Figure 1 steps 1 and 3). The spatially uniform root mean square error (RMSE) was calculated using a subset of test-points from our case study that were close to the active channel as:

$$RMSE = \left[\frac{\sum_{j=1}^{n} \varepsilon_j^2}{n}\right]^{0.5}, \#(5)$$

where n is the number of test-points and ε_j is the linear distance between the j^{th} test-point in the transformed warp image (x_j', y_j') and the base image (x_j, y_j), calculated as:

$$\varepsilon_j = \left[\left(x_j - x_j'\right)^2 + \left(y_j - y_j'\right)^2\right]^{0.5}. \#(6)$$

We used a subset of test-points close to the active channel to eliminate the influence of unusually large test-point errors located on adjacent hillslopes that were automatically selected by the area-based matching algorithm and would not have affected channel change measurements. The RMSEs for 1954 and 1961 were 4.95 and 4.52 m, respectively. We assumed that the maximum digitizing uncertainty in our case study was 2 m based on previous studies (Donovan et al, 2019) and defined the digitizing uncertainty using a normal distribution with a mean of zero and a standard deviation of 2/3, as described in Section 2 (Figure 1 step 4).

Interpretation uncertainty was estimated by separately digitizing the minimum and maximum extent of the active channel and vegetated islands (Figure 1 step 2). For our case study, we used an initial threshold of 10% vegetation density to classify surfaces as channel (<10% vegetation density) or floodplain (>10% vegetation density). However, we were uncertain in several locations whether a surface with >10% vegetation had aggraded to a height similar to that of the surrounding floodplain with denser, more mature vegetation because the images were not viewed in stereo. This sort of uncertainty is inevitable in any channel change study but the A_{min} and A_{max} boundaries described in Section 2 provided a means of classifying these uncertain surfaces as both active channel and floodplain.

We also used a sequence of aerial images that were collected before and after the image being digitized to help us understand the evolution of alluvial surfaces with interpretation uncertainty through time. For example, if an ambiguous surface showed a clear evolution from an unambiguous active channel in the earlier image to unambiguous floodplain in the later image, we knew that during the image sequence the surface changed from channel to floodplain and assumed that the ambiguous surface in the intermediate image being digitized was within this gradual transition. In this instance, we would use the A_{min} and A_{max} bounds to classify the surface as both channel and floodplain. Conversely, if the surface was unambiguously active channel in both the earlier and later images, we would assume that the surface in the intermediate image being digitized was also active channel and the increase in vegetation on that surface might have been caused by the proliferation of vegetation on bars during a period when the annual snowmelt floods were small.

Figure 6 presents two examples from our case study where we used a sequence of aerial images to guide our interpretation of ambiguous alluvial surfaces. The partly vegetated surface in Figure 6 a,b is an example of a vegetated island where the secondary back channel was unambiguously part of the active channel in an image from 1938 and unambiguously part of the floodplain in an image from 1975, but in the 1954 and 1961 images, there was ambiguity in whether the surface was the channel or floodplain. This interpretation uncertainty implied that the surface could be classified as a vegetated island in A_{max} (Figure 6a) or as part of the floodplain in A_{min} (Figure 6b). Similarly, Figure 6c,d is an example of a vegetated bank-attached bar that was unambiguously active channel in the 1938 image and unambiguously floodplain in the 1975 image, but there was ambiguity in whether the surface was floodplain or channel in the 1954 and 1961 images. Therefore, the surface was included as part of the active channel in the A_{max} delineation (Figure 6c) and part of the floodplain in the A_{min} delineation (Figure 6d).

The net planform change was calculated as the amount of erosion subtracted from the amount of deposition, with positive values indicating net deposition and negative values indicating net erosion. The total net planform change using the SDP method, as evaluated in our case study, was calculated by overlaying the probabilistic delineations in 1954 and 1961 to create a distribution of erosion and deposition polygons for each A_{Max} and A_{Min} overlay and then merging the net planform change from all A_{Max} and A_{Min}

overlays (Figure 1 step 7) into a single probability distribution. This distribution represented the combined uncertainty associated with co-registration, digitization, and interpretation. We also normalized the distribution of net planform change by dividing the net areal change by the channel centerline length to facilitate interpretation and comparison among reaches. For example, if the magnitude of net change was 100 m^2 of erosion and the channel length was 10 m, the normalized net change would be 10 m of erosion for every downstream meter, which we would consider a large amount of erosion. Conversely, if this amount of areal change occurred over a channel length of 10,000 m, the normalized net change would only be 0.1 m of erosion per a downstream meter, which we would consider a small amount of erosion. Additionally, normalizing the net planform change by the channel centerline length allowed us to interpret the results in terms of net changes in channel width. In case studies where multiple sets of aerial images are used, the net planform change should also be normalized by the number of years between each set of aerial images so that the magnitude of change between image pairs is comparable; this form of standardization would also aid in comparing channel change case studies from the literature.

3.2. Comparison of the SDP method with existing methods of characterizing channel change uncertainty

The uncertainty inherent to measurements of channel change from aerial images implies that any channel change analysis must consider the impact of these uncertainties on the results. We evaluated whether the SDP method improved upon previous methods by comparing the results from our case study when the uncertainty was quantified using the SDP method and two existing methods that used a spatially uniform image co-registration error and did not characterize the uncertainty probabilistically. The first method (ε_1) was similar to that of Urban and Rhoads (2003) and Micheli and Kirchner (2002) in that we created an uncertainty bound with a width of the propagated co-registration error and digitization uncertainty using:

$$\varepsilon_1 = \left[rmse_{t1}{}^2 + rmse_{t2}{}^2 + \varepsilon_{digitizing}{}^2\right]^{0.5};\#(7)$$

where $rmse_{t1}$ and $rmse_{t2}$ were the spatially uniform co-registration errors for each image (i.e., 4.95 and 4.52 m for the 1954 and 1961 images, respectively) and $\mathcal{E}_{digitizing}$ was the maximum digitization uncertainty, which we assumed to be 2 m. The maximum area for each erosional or depositional polygon was the area of the $\mathcal{E}_1$ uncertainty band added to the original polygon (Figure 7a-c), and the minimum area was the $\mathcal{E}_1$ uncertainty band subtracted from the original polygon (Figure 7d-f). The minimum net planform change was the sum of the maximum area of erosion for all polygons (Figure 7c) subtracted from the sum of the minimum area of deposition (Figure 7f). The maximum net planform change was the sum of the minimum area of erosion (Figure 7f) subtracted from the sum of the maximum area of deposition (Figure 7c).

The second method (ε_2) was developed by Swanson et al. (2011) and involved estimating uncertainty in the width of each polygon of erosion and deposition using equation 7 and converting the width uncertainty to an area by multiplying by the polygon length. The total magnitude of uncertainty in erosion or deposition was the sum of uncertainty across all erosional or depositional polygons, and the minimum and maximum bounds for net planform change were calculated in the same way as for ε_1.

3.3. Results: Comparison of methods to quantify the uncertainty associated with channel change

The output from the SDP method was a distribution of planform change that we used to calculate the probability that net change in our case study was erosional or depositional along with a 95% credible interval as a summary metric of uncertainty. The 95% credible interval contained 95% of the most probable values and thus provided a measure of uncertainty comparable to the spatially uniform $\mathcal{E}_1$ and $\mathcal{E}_2$ methods. We suggest that the 95% credible interval could be a useful metric of uncertainty in other studies that are not necessarily focused on directly comparing uncertainty methods, as was the main objective of our case study.

The SDP method, as implemented in our case study, significantly reduced the magnitude of uncertainty in measurements of areal channel change compared to the $\mathcal{E}_1$ and $\mathcal{E}_2$ methods. The maximum extents of erosion and deposition using the $\mathcal{E}_1$ method (Figure 8a) were greater than the maximum extents using the SDP method (Figure 8c) because the $\mathcal{E}_1$ uncertainty bound (Equation 7) was generally larger than the local probabilistic delineation of the channel extent generated by the SDP method. Conversely, the minimum extent of erosion and deposition using the $\mathcal{E}_1$ method (Figure 8b) was much smaller than the SDP method (Figure 8d) because $\mathcal{E}_1$ uncertainty band was greater than the size of several polygons, which caused those polygons to be completely removed from the $\mathcal{E}_1$ minimum extent (Figure 8b). The combined effect of these differences was a reduction in the uncertainty of deposition by 72% and 78% relative to $\mathcal{E}_1$ and $\mathcal{E}_2$, respectively, and in erosion by 84% and 87% relative to $\mathcal{E}_1$ and $\mathcal{E}_2$, respectively (Figure 8c,d inset; Table 1). The negative minimum bound of erosion and deposition in the $\mathcal{E}_2$ method (Table 1; inset Figure 8c,d) had no physical meaning because the amount of erosion and deposition could not be less than zero. This spurious result was caused by the uncertainty being greater than the planform change (e.g., $A_{Max(t1)}$&$A_{Min(t2)}$ deposition was 6.5 ± 14.0; Table 1).

In our case study, we could not conclude with confidence whether the channel margins or vegetated islands accumulated or evacuated sediment, nor the direction of the total net planform change, using the $\mathcal{E}_1$ and $\mathcal{E}_2$ methods, because the uncertainty band spanned zero (Figure 9). Although the SDP 95% credible interval also spanned zero, the results were more informative, because we could estimate the probability of change. More specifically, we found a 37% probability that the total net planform change was depositional (Figure 9a; Table 1), a 19% probability that the channel boundary accumulated sediment (Figure 9b; Table 1), and a 100% probability that vegetated islands accumulated sediment (Figure 9c; Table 1). Also, the magnitude of the 95% credible interval associated with the distribution generated by the SDP method was 80% and 78% smaller than the $\mathcal{E}_1$ and $\mathcal{E}_2$ uncertainty bounds, respectively (Table 1). Thus, the SDP method significantly reduced the bound of uncertainty compared to the $\mathcal{E}_1$ and $\mathcal{E}_2$ methods.

The distribution of change generated from the SDP method provided a quantitative basis for deciding whether the probability of change in our case study was large enough to support meaningful geomorphic conclusions. For the purposes of this case study, there was an inconsequential risk associated with accepting the channel change results as true change when the change might have been caused by co-registration error or digitization and interpretation uncertainty, so we decided that a 19%

probability of deposition along the channel boundary was sufficient to justify the conclusion that the channel boundary evacuated sediment. Similarly, we concluded that the vegetated islands accumulated sediment based on a 100% probability of vegetated island deposition. Overall, the net channel change was erosional rather than depositional based on a 37% probability that the net change was depositional. Conversely, the only conclusion that could be made for our case study based on the $\mathcal{E}_1$ and $\mathcal{E}_2$ method was that the results implied an indeterminate net sediment balance.

3.3.1. The relative magnitude of each type of error and uncertainty

The SDP method processes each source of error and uncertainty individually, which avoids the requirement that errors and uncertainties be normally distributed with a mean of zero for error propagation. This is an important improvement to the $\mathcal{E}_1$ and $\mathcal{E}_2$ methods that incorrectly assume that the RMSE has a mean error of zero. Additionally, processing uncertainties individually allowed us to assess the net effect of each type of uncertainty on channel change to identify the primary driver of uncertainty in our case study. Such an analysis could not have been performed using traditional methods that rely on error propagation.

The magnitude of the co-registration error in our case study was defined by extracting $\|\overrightarrow{\varepsilon_{xy}}\|$ from each A_{max} and A_{min} vertex for the 10 error surfaces. The magnitude of the digitization uncertainty was simply the normal distribution defined in Section 3.1 as having a mean of zero and a standard deviation of 2/3. Interpretation uncertainty was calculated as the difference between the minimum and maximum active channel areas in our study reach calculated within 150 channel-spanning cells spaced at 150-m streamwise intervals along the channel centerline. The difference in area within each cell was normalized by the channel centerline length, which allowed us to express the interpretation uncertainty in units of length comparable to the co-registration error and digitization uncertainty.

In our case study, co-registration was the largest source of error, followed by interpretation and digitization uncertainty (Figure 10). The median of the image co-registration error was larger than the interpretation uncertainty (3.0 vs. 0.0 m), but the mean was comparable (3.7 vs. 3.3 m). By definition, the mean of the digitization uncertainty was 0 m and smaller than interpretation uncertainty and co-registration error. The median of the interpretation uncertainty was extremely small because in 56% of the study area the extent of the channel boundary was unambiguous. Conversely, the co-registration error was greater than zero throughout the entire study area. If we only considered cells where the interpretation uncertainty was greater than 0 m, the median interpretation uncertainty increased to 2.4 m and the mean increased to 7.4 m. The results of our case study suggest that interpretation uncertainty can be much larger than any other source of uncertainty, implying that interpretation uncertainty should be considered in all studies of channel change. However, we emphasize that the results presented here are unique to our case study and that the magnitude of each source of uncertainty could be different in other studies.

3.3.2. Net effect of interpretation uncertainty

The overall effect of interpretation uncertainty in our case study was characterized by individually examining the net change in different A_{max} and A_{min} overlays and we found that different A_{max} and A_{min} overlays tended toward net erosion or deposition (Figure 11). The difference was greatest when A_{Min} and A_{Max} were overlaid: $A_{Max(t1)}$&$A_{Min(t2)}$ had a 90% probability of net deposition whereas $A_{Min(t1)}$&$A_{Max(t2)}$ only had a 1% probability of net deposition (Figure 11a,b; Table 1). We attributed this result to the $A_{Max(t1)}$&$A_{Min(t2)}$ overlay favoring net deposition along the channel margins and vegetated islands (Figure 12), which created a high probability that the net planform change was depositional (Figure 11a). The magnitude of vegetated island deposition was smaller for the $A_{Min(t1)}$&$A_{Max(t2)}$ overlay (Figure 12a) and sediment was evacuated from the channel margin (Figure 12b), decreasing the probability that net planform change was depositional for the $A_{Min(t1)}$&$A_{Max(t2)}$ overlay (Figure 11b). The net planform change along the channel margins and vegetated islands differed little between the $A_{Max(t1)}$&$A_{Max(t2)}$ and $A_{Min(t1)}$&$A_{Min(t2)}$ overlays (Figure 12), and the probability that each overlay was depositional was similar (Figure 11c,d). Thus, the $A_{Max(t1)}$&$A_{Max(t2)}$ and $A_{Min(t1)}$&$A_{Min(t2)}$ overlays represented the most conservative amount of channel change and the probability of this scenario occurring in the overall distribution of net change was 50%. Conversely, the $A_{Min(t1)}$&$A_{Max(t2)}$ and $A_{Max(t1)}$&$A_{Min(t2)}$ overlays represented the most extreme amount of deposition or erosion and each of these scenarios had a 25% chance of occurring in the overall distribution of net change.

4. Discussion

Numerous studies have analyzed repeat aerial images to detect channel change, but the lack of a consistent methodology to quantify and incorporate uncertainty has led to the use of many methods for estimating uncertainty in measurements of channel change with varying degrees of rigor and complexity (Gurnell et al., 1994; Winterbottom and Gilvear, 1997; Mount et al., 2003; Mount and Louis, 2005). Previous methods to quantify uncertainty could only be applied to one type of channel change measurement (i.e., linear channel adjustments or polygons of change), which prevents these methods from being applicable to all channel change studies. The SDP method presented here is the first generalizable method for characterizing uncertainty associated with measurements of channel change that can be used with all forms (i.e., both linear and areal metrics) of channel change measurements from an image time series.

The SDP method improves upon other methods of quantifying uncertainties by estimating planform change probabilistically, rather than specifying a LoD threshold and discarding measured changes less than this threshold (Winterbottom and Gilvear, 1997; Martin, 2003; Urban and Rhoads, 2003; Surian et al., 2009; White et al., 2010; De Rose and Basher, 2011; Kessler et al., 2013). By avoiding the use of a LoD threshold, the SDP method retains all polygons of channel change and calculates a distribution of each polygon's area given the uncertainty. The retention of all channel change measurements is a significant improvement to previous methods that discard changes smaller than a threshold because all polygons of change, whether small or large, contribute to our understanding of the processes and mechanisms by which channels adjust. Additionally, eliminating the LoD threshold has the potential to significantly improve the accuracy of channel change studies that use bank line retreat to estimate volumes of bank erosion (Rhoades et al., 2009; De Rose and Basher, 2011; Day et al., 2013; Kessler et al., 2013), because point bars are commonly constructed to a lower elevation than eroding cutbanks (Lauer and Parker, 2008) and slivers of bank retreat removed by the LoD threshold can sum to large volumes of erosion when they extend over a large area and are multiplied by the bank height.

The case study presented in this paper demonstrated that the SDP method can significantly reduce the uncertainty in measurements of channel change from repeat aerial images. While the SDP method is rigorous and robust, the technique is computationally intensive. For example, in our case study we sampled our probabilistic distributions 5,000 times to create a distribution of 20,000 channel change measurements and the runtime for this analysis was ~20 minutes on a computer with 32 gigabytes of RAM and a 3.70 GHz processor. In comparison, the runtime for the $\mathcal{E}_1$ and $\mathcal{E}_2$ methods was less than 1 minute.

One way to decrease the SDP processing time is to reduce the number of randomly sampled channel boundary delineations used to calculate the distribution of channel change measurements (Figure 1 step 6). To test the sensitivity of the distribution of channel change to sample size, we ran the SDP method using a range of sample sizes from 1,000 to 10,000. This sensitivity analysis showed that the distributions of channel change measurements were similar for all sample sizes (Figure 13), implying that we could have reduced the number of samples to 1,000 without significantly changing our results. If computation time is a concern in other studies, we suggest performing a similar sensitivity analysis on a subset of the study area to determine the optimal number of sampled boundary delineations used to create the distribution of channel change.

4.1. When to use the SDP method

Not all channel change studies require a method as rigorous and robust as the SDP method to quantify uncertainty. We suggest that the level of complexity and rigor appropriate for any effort to detect channel change depends on three factors: the magnitude of uncertainty compared to the magnitude of channel change, the objective of the study, and the amount of time between the aerial images used to detect change.

In small rivers, the uncertainty can be a large proportion of the total channel area (Swanson et al., 2011) and channel change may need to be quite large (e.g., greater than 25% of the width of the channel) compared to the size of the river to overcome the geospatial uncertainty. In such instances, the smaller bound of uncertainty produced by the SDP method will increase the likelihood of detecting channel change. When the signal of channel change is extremely large, as in laterally unstable rivers, a less complex uncertainty characterization method might be suitable regardless of the channel size (e.g., Surian, 1999; Cadol et al., 2011; Ziliani and Surian, 2012; Moretto et al., 2014; Righini et al., 2017).

We identified two sites of bank erosion from our channel change case study where channel change was large enough that a less robust uncertainty method could be used and where channel change was small and only detectable by the SDP method. Bank erosion at both sites was visible by comparing the 1954 to 1961 aerial images but the $\mathcal{E}_1$ and $\mathcal{E}_2$ methods produced an indeterminate result when the magnitude of erosion was small, whereas the SDP method could detect this small erosional signal (Figure 14a,b). Conversely, the $\mathcal{E}_1$, $\mathcal{E}_2$, and SPD methods could all detect bank erosion when the signal was large (Figure 14c,d). This example from our case study highlights the benefit of using the SDP method when the signal of channel change is small compared to the uncertainty.

When the study objective is to calculate the absolute magnitude of planform change, rather than the direction of change as erosional or depositional, the SDP method significantly reduces the uncertainty bound (Table 1) and enables a more precise estimate of the magnitude of channel change. We demonstrate this capability using the two sites of bank erosion from our channel change case study discussed above (Figure 14). The $\mathcal{E}_1$ and $\mathcal{E}_2$ methods predicted anywhere from 0.65 m of deposition to 15 m of erosion at the site with a smaller amount of bank erosion, whereas the SDP method predicted 3.5 to 8 m of bank erosion (Figure 14a,b). At the site with a larger amount of bank erosion, there was anywhere from 2 to 28 m of erosion using the $\mathcal{E}_1$ and $\mathcal{E}_2$ methods but that uncertainty bound was reduced to 13 to 18 m of erosion using the SDP method (Figure 14c,d). These examples demonstrate how well the SDP method can constrain the magnitude of channel change, and we suggest that this method be used when the study objective is to calculate the absolute magnitude of change.

Lastly, the temporal interval between aerial images compared to the activity of the channel during that interval will govern the amount of channel change recorded and, therefore, the type of uncertainty analysis needed to detect significant channel change. When aerial images are acquired in closely spaced time intervals and channel change is small (e.g., Manners et al., 2014), the SDP method might facilitate channel change detection. Conversely, when channel changes are large, significant channel change might be detectable with a less robust form of uncertainty analysis, regardless of the time interval between aerial images.

4.2. When does each type of error and uncertainty matter?

In the SDP method, we distinguish between error and uncertainty by defining error as a deviation from a known value and uncertainty as a range of values that encompasses the true measurement. One advantage of the SDP method is that errors and uncertainties are added individually rather than being propagated to a single value, and by doing so, the user can evaluate the relative magnitude of each source of error and uncertainty and assess the effects on the channel change analysis. In our case study, co-registration error was the greatest source of error, followed by interpretation and digitization uncertainty (Figure 10), but the significance of each type of uncertainty might be different in other study areas, or within the same study area when using different aerial images. In the following sections, we describe scenarios when each source of uncertainty is significant and other scenarios when that type of uncertainty might be disregarded. Understanding which sources of uncertainty are important in a given study can help guide the selection of an appropriate uncertainty method.

4.2.1. *Spatially distributed image co-registration error*

Image co-registration error is relevant when two images are overlaid to calculate planform change. When planform metrics are derived from a single image (e.g., width and active channel area), the co-registration error is irrelevant, because the images are not overlaid, although image distortion can still cause uncertainty in these planform metrics if the images are not orthorectified. The co-registration error can be quantified as uniform across the study area using the RMSE (Equation 5) of tie-points used to warp the image, the RMSE (Equation 5) of independent test-points, or the co-registration error can be allowed to vary spatially, as done in the SDP method (Figure 1 step1). When planform change is small (e.g., less than 25% of the width of the channel), a spatially variable co-registration error is necessary, because this error is often lower than the uniform RMSE near the channel, which allows smaller planform changes to be detected. In our case study, using a spatially variable co-registration error reduced the error at ~83% of the A_{min} and A_{max} vertices in the 1954 and 1961 images (Figure 15) and shrunk the overall uncertainty bounds by 78-90% (Table 1). If the planform change is extremely large, the uniform RMSE might be small compared to the channel change signal and a spatially variable co-registration error would not be necessary. To decide whether the co-registration error should be allowed to vary spatially, the magnitude of uncertainty in the ε_1 method can be compared to estimated planform change when uncertainty is not considered. If the ε_1 uncertainty bound is greater than the magnitude of change, co-registration error should be allowed to vary spatially.

The effectiveness of the spatially variable co-registration error in reducing uncertainty will depend on the number, distribution, and quality of test-points. We suggest using an automated procedure to generate test-points throughout the study area (e.g., Carbonneau et al., 2010) and supplementing those test-points with manually selected test-points near the channel. Additionally, the user could test the sensitivity of the SDP method to the number, density, and distribution of test-points in their study area.

4.2.2. *Digitization uncertainty*

Digitization uncertainty is affected by the spatial and spectral resolution of the image. The spatial resolution determines the smallest object that can be observed in an image. The appropriate spatial resolution for a channel change analysis will depend on the channel dimensions and might vary within the study area. If the spatial resolution is low and the channel is narrow, a single pixel may contain a portion of the active channel and the channel boundary, introducing uncertainty as to where to place the boundary within the pixel. The greater the proportion of pixels that contain both the active channel and the channel boundary, the larger the digitization uncertainty. Spectral resolution refers to the range of wavelengths within each one of the sensor's spectral bands. Aerial images collected by sensors with a high spectral resolution are more likely to have a near-infrared wavelength band. This type of band is helpful, because the near-infrared wavelength can be used to distinguish the boundary between vegetation, water, and bare channel bars, which reduces the digitization uncertainty.

The crispness of the boundary can also affect digitizing uncertainty. Easily identifiable features with sharp boundaries, like roads or buildings, will have a smaller digitizing uncertainty than fuzzy boundaries that are less crisp, such as trees. Along rivers in arid regions with little vegetation, actively eroding banks create crisp boundaries and have low digitizing uncertainty. In humid or mountainous regions, vegetation along the channel boundary is denser and eroding banks cause trees to fall into the channel, making the boundary fuzzier and subject to larger digitizing uncertainty. Shadows can cause crisp boundaries to become fuzzy during certain times of the day; digitization uncertainty is thus sensitive to flight timing.

Most study areas contain both crisp and fuzzy boundaries, which will cause the digitizing uncertainty to vary spatially. Currently, a spatially variable digitizing uncertainty has not been used in a channel change study; this is an area for future work. Although the SDP method does not directly incorporate a spatially variable digitizing uncertainty, the distribution used to describe the digitizing uncertainty can be adjusted to account for fuzzy and crisp boundaries by increasing the standard deviation or creating a mixed normal distribution. In this way, the SDP method is a significant improvement to previous methods that use a single value to define digitizing uncertainty.

4.2.3. *Interpretation uncertainty*

Interpretation uncertainty occurs when there are different plausible interpretations of the extent of the active channel. If the channel boundary can be identified based on breaks in topography from stereo images or digital elevation models, the interpretation uncertainty will tend to be smaller. However, freely available aerial images that are regularly acquired typically are not collected in stereo, and current practice involves delineating channel boundaries in GIS software without the aid of stereo images.

In our case study, interpretation uncertainty was a large source of uncertainty in some localized areas, but there was no uncertainty elsewhere. This caused the median of this uncertainty to be small (Figure 10; 0.00 m), because the uncertainty was not present in 56% of the study area. In other case studies, interpretation uncertainty might be small in localized areas or more pervasive throughout the study area. We suspect that interpretation uncertainty will be high in rivers that experience a large change in wetted channel area given a proportionately small change in discharge (e.g., braided rivers), because low-elevation bars are frequently wetted but not scoured, which allows fast-growing vegetation to encroach on these surfaces (Werbylo et al., 2017). In such rivers, vegetation density is a poor proxy for the active channel, and the digitizer must use professional judgment in placing the active channel boundary. Similarly, vegetation might be a poor indication of the channel extent in rivers that experience flashy hydrology or that are subjected to large reset floods and very low base flows, because there might be a mosaic of bare alluvial surfaces at multiple elevations after a large flood that are hard to interpret (Dean and Schmidt, 2011, 2013; Thompson and Croke, 2013). Additionally, in humid environments where plants grow quickly, vegetation growing in the active channel during base flow can introduce ambiguity.

Interpretation uncertainty is likely to be larger for channels that are narrowing as compared to those that are widening. Channels widen through bank erosion that removes an entire section of sediment and creates an abrupt, crisp contact between the channel and floodplain with minimal interpretation uncertainty. Conversely, channel narrowing occurs over a continuum as alluvial surfaces transition from active channel bars to floodplains by vertically aggrading sediment (Allred and Schmidt, 1999; Grams and Schmidt, 2002; Moody et al., 1999; Pizzuto, 1994). Determining when enough sediment has accumulated on an alluvial surface to form a stable floodplain that is inundated by floods of an annual or greater recurrence is highly uncertain and subject to large interpretation uncertainty.

5. Conclusions

In this paper, we introduced a new method for quantifying uncertainty associated with channel change detection based on probabilistic, spatially varying estimates of co-registration error and digitization uncertainty. We also presented a framework that can be used to incorporate interpretation uncertainty into the channel change analysis. The SDP method can be used to calculate uncertainty at specific locations of linear channel adjustment or polygons of erosion and deposition, while also estimating the central tendency of net planform change, making this the first generalizable method for quantifying uncertainty that can be applied to all metrics of channel change derived from aerial image overlays. Although the focus of this paper was the detection of channel change, the SDP method can be applied to other geomorphic and landscape change detection analyses, such as glacial change (DeVisser and Fountain, 2015), shoreline or tidal wetland change (Del Río et al., 2013), and changes in water body surfaces (Necsoiu et al., 2013).

The SDP method as applied to our case study reduced the magnitude of uncertainty by 83-87% compared to two existing methods that used a spatially uniform image co-registration error and did not characterize uncertainty probabilistically. By reducing the bounds of uncertainty, we were able to detect channel changes of a smaller magnitude. More importantly, the distribution information from the SDP method allowed us to report a magnitude of channel change in our case study with an appropriate level of confidence even though the uncertainty bound included zero. We could not make a similar inference using the existing methods, because their uncertainty bounds had no distribution information and included zero, making the results indeterminate.

The SDP method was an improvement to existing methods that quantify uncertainty without distributional information, but the method was computationally intensive and might not be necessary for all change detection studies. We suggest that the SDP method should be used in channel change studies where 1) the uncertainty is a large proportion of the total channel area, as in small rivers; 2) when the temporal spacing between aerial images is short and the channel change is expected to be small; and 3) when the purpose of the study is to calculate the absolute magnitude of change, such as studies that use bank retreat to calculate the volume of bank erosion.

Acknowledgments

The work by the first author was supported by the Colorado River Doctoral Scholar program of the Center for Colorado River Studies at Utah State University and by the Babbitt Center for Land and Water Policy. Any use of trade, firm, or product names is for descriptive purposes only and does not imply endorsement by the U.S. Government.

Data Availability

A MATLAB® script for performing an SDP uncertainty analysis is available at https://qcnr.usu.edu/coloradoriver/files/leonard_data. The data used in this case study are available from the U.S. Geological Survey (USGS) ScienceBase at https://doi.org/10.5066/P9SEBJ3X (Legleiter and Leonard, 2020).

References

Agisoft LLC. 2016. Agisoft Photoscan Professional edition

Allred TM, Schmidt JC. 1999. Channel narrowing by vertical accretion along the Green River near Green River, Utah. GSA Bulletin **111** : 1757–1772. DOI: 10.1130/0016-7606(1999)111<1757:CNBVAA>2.3.CO;2

Amidror I. 2002. Scattered Data Interpolation Methods for Electronic Imaging Systems: A Survey. Journal of Electronic Imaging **11** : 157–176. DOI: 10.1117/1.1455013

Anderson S, Pitlick J. 2014. Using repeat LiDAR to estimate sediment transport in a steep stream. Journal of Geophysical Research: Earth Surface **119** : 621–643. DOI: 10.1002/2013JF002933

Anderson SW. 2019. Uncertainty in quantitative analyses of topographic change: error propagation and the role of thresholding. Earth Surface Processes and Landforms **44** : 1015–1033. DOI: 10.1002/esp.4551

Andrews E. 1980. Effective and bankfull discharges of streams in the Yampa River basin, Colorado and Wyoming. Journal of Hydrology **46** : 311–330. DOI: 10.1016/0022-1694(80)90084-0

Best J. 2019. Anthropogenic stresses on the world's big rivers. Nature Geoscience **12** : 7–21. DOI: 10.1038/s41561-018-0262-x

Bollati IM, Pellegrini L, Rinaldi M, Duci G, Pelfini M. 2014. Reach-scale morphological adjustments and stages of channel evolution: The case of the Trebbia River (northern Italy). Geomorphology **221** : 176–186. DOI: 10.1016/j.geomorph.2014.06.007

Brasington J, Langham J, Rumsby B. 2003. Methodological sensitivity of morphometric estimates of coarse fluvial sediment transport. Geomorphology **53** : 299–316. DOI: 10.1016/S0169-555X(02)00320-3

Buckingham SE, Whitney JW. 2007. GIS Methodology for Quantifying Channel Change in Las Vegas, Nevada. JAWRA Journal of the American Water Resources Association **43** : 888–898. DOI: 10.1111/j.1752-1688.2007.00073.x

Cadol D, Rathburn SL, Cooper DJ. 2011. Aerial photographic analysis of channel narrowing and vegetation expansion in Canyon De Chelly National Monument, Arizona, USA, 1935–2004. River Research and Applications **27** : 841–856. DOI: 10.1002/rra.1399

Carbonneau PE, Dugdale SJ, Clough S. 2010. An automated georeferencing tool for watershed scale fluvial remote sensing. River Research and Applications **26** : 650–658. DOI: 10.1002/rra.1263

Comiti F, Da Canal M, Surian N, Mao L, Picco L, Lenzi MA. 2011. Channel adjustments and vegetation cover dynamics in a large gravel bed river over the last 200 years. Geomorphology **125** : 147–159. DOI: 10.1016/j.geomorph.2010.09.011

Day SS, Gran KB, Belmont P, Wawrzyniec T. 2013. Measuring bluff erosion part 2: pairing aerial photographs and terrestrial laser scanning to create a watershed scale sediment budget. Earth Surface Processes and Landforms **38** : 1068–1082. DOI: 10.1002/esp.3359

De Rose RC, Basher LR. 2011. Measurement of river bank and cliff erosion from sequential LIDAR and historical aerial photography. Geomorphology **126** : 132–147. DOI: 10.1016/j.geomorph.2010.10.037

Dean DJ, Schmidt JC. 2011. The role of feedback mechanisms in historic channel changes of the lower Rio Grande in the Big Bend region. Geomorphology **126** : 333–349. DOI: 10.1016/j.geomorph.2010.03.009

Dean DJ, Schmidt JC. 2013. The geomorphic effectiveness of a large flood on the Rio Grande in the Big Bend region: Insights on geomorphic controls and post-flood geomorphic response. Geomorphology **201** : 183–198. DOI: 10.1016/j.geomorph.2013.06.020

Del Río L, Gracia FJ, Benavente J. 2013. Shoreline change patterns in sandy coasts. A case study in SW Spain. Geomorphology **196** : 252–266. DOI: 10.1016/j.geomorph.2012.07.027

DeVisser MH, Fountain AG. 2015. A century of glacier change in the Wind River Range, WY. Geomorphology **232** : 103–116. DOI: 10.1016/j.geomorph.2014.10.017

Donovan M, Belmont P. 2019. Timescale dependence in river channel migration measurements. Earth Surface Processes and Landforms **44** : 1530–1541. DOI: 10.1002/esp.4590

Donovan M, Belmont P, Notebaert B, Coombs T, Larson P, Souffront M. 2019. Accounting for uncertainty in remotely-sensed measurements of river planform change. Earth-Science Reviews **193** : 220–236. DOI: 10.1016/j.earscirev.2019.04.009

Downward SR, Gurnell AM, Brookes A. 1994. A methodology for quantifying river channel planform change using GIS. IAHS Publications-Series of Proceedings and Reports-Intern Assoc Hydrological Sciences **224** : 449–456.

Gaeuman D, Symanzik J, Schmidt JC. 2005. A map overlay error model based on boundary geometry. Geographical Analysis **37** : 350–369. DOI: 10.1111/j.1538-4632.2005.00585.x

Gaeuman DA, Schmidt JC, Wilcock PR. 2003. Evaluation of in-channel gravel storage with morphology-based gravel budgets developed from planimetric data. Journal of Geophysical Research: Earth Surface **108** : 6001. DOI: 10.1029/2002JF000002

Grams PE, Schmidt JC. 2002. Streamflow regulation and multi-level flood plain formation: channel narrowing on the aggrading Green River in the eastern Uinta Mountains, Colorado and Utah. Geomorphology **44** : 337–360. DOI: 10.1016/S0169-555X(01)00182-9

Grams PE, Schmidt JC. 2005. Equilibrium or indeterminate? Where sediment budgets fail: Sediment mass balance and adjustment of channel form, Green River downstream from Flaming Gorge Dam, Utah and Colorado. Geomorphology **71** : 156–181. DOI: 10.1016/j.geomorph.2004.10.012

Gurnell AM, Downward SR, Jones R. 1994. Channel planform change on the River Dee meanders, 1876–1992. Regulated Rivers: Research & Management **9** : 187–204. DOI: 10.1002/rrr.3450090402

Ham DG, Church M. 2000. Bed-material transport estimated from channel morphodynamics: Chilliwack River, British Columbia. Earth Surface Processes and Landforms **25** : 1123–1142. DOI: 10.1002/1096-9837(200009)25:10<1123::AID-ESP122>3.0.CO;2-9

Hughes ML, McDowell PF, Marcus WA. 2006. Accuracy assessment of georectified aerial photographs: implications for measuring lateral channel movement in a GIS. Geomorphology **74** : 1–16. DOI: 10.1016/j.geomorph.2005.07.001

Kessler AC, Gupta SC, Brown MK. 2013. Assessment of river bank erosion in Southern Minnesota rivers post European settlement. Geomorphology **201** : 312–322. DOI: 10.1016/j.geomorph.2013.07.006

Lauer JW, Parker G. 2008. Net local removal of floodplain sediment by river meander migration. Geomorphology **96** : 123–149. DOI: 10.1016/j.geomorph.2007.08.003

Lea DM, Legleiter CJ. 2016. Refining measurements of lateral channel movement from image time series by quantifying spatial variations in registration error. Geomorphology **258** : 11–20. DOI: 10.1016/j.geomorph.2016.01.009

Legleiter CJ. 2014. Downstream Effects of Recent Reservoir Development on the Morphodynamics of a Meandering Channel: Savery Creek, Wyoming, Usa. River Research and Applications : 1328–1343. DOI: 10.1002/rra.2824

Legleiter CJ, Leonard CM. 2020. Aerial photographs from the Yampa and Little Snake Rivers in northwest Colorado used to characterize channel changes occuring between 1954 and 1961. U.S. Geological Survey data release [online] Available from: https://doi.org/10.5066/P9SEBJ3X

Leonard C, Legleiter C, Overstreet B. 2017. Effects of lateral confinement in natural and leveed reaches of a gravel-bed river: Snake River, Wyoming, USA. Earth Surface Processes and Landforms **42** : 2119–2138. DOI: 10.1002/esp.4157

Lyons JK, Pucherelli MJ, Clark RC. 1992. Sediment transport and channel characteristics of a sand-bed portion of the Green River below Flaming Gorge Dam, Utah, USA. Regulated Rivers: Research & Management **7** : 219–232. DOI: 10.1002/rrr.3450070302

Magilligan FJ, Haynie HJ, Nislow KH. 2008. Channel Adjustments to Dams in the Connecticut River Basin: Implications for Forested Mesic Watersheds. Annals of the Association of American Geographers **98** : 267–284. DOI: 10.1080/00045600801944160

Manners RB, Schmidt JC, Scott ML. 2014. Mechanisms of vegetation-induced channel narrowing of an unregulated canyon river: Results from a natural field-scale experiment. Geomorphology **211** : 100–115. DOI: 10.1016/j.geomorph.2013.12.033

Martin DJ, Pavlowsky RT. 2011. Spatial Patterns of Channel Instability Along an Ozark River, Southwest Missouri. Physical Geography **32** : 445–468. DOI: 10.2747/0272-3646.32.5.445

Martin Y. 2003. Evaluation of bed load transport formulae using field evidence from the Vedder River, British Columbia. Geomorphology **53** : 75–95. DOI: 10.1016/S0169-555X(02)00348-3

Merritt DM, Cooper DJ. 2000. Riparian vegetation and channel change in response to river regulation: a comparative study of regulated and unregulated streams in the Green River Basin, USA. Regulated Rivers: Research & Management **16** : 543–564. DOI: 10.1002/1099-1646(200011/12)16:6<543::AID-RRR590>3.0.CO;2-N

Micheli ER, Kirchner JW. 2002. Effects of wet meadow riparian vegetation on streambank erosion. 1. Remote sensing measurements of streambank migration and erodibility. Earth Surface Processes and Landforms **27** : 627–639. DOI: 10.1002/esp.338

Moody JA, Pizzuto JE, Meade RH. 1999. Ontogeny of a flood plain. GSA Bulletin **111** : 291–303. DOI: 10.1130/0016-7606(1999)111<0291:OOAFP>2.3.CO;2

Moretto J, Rigon E, Mao L, Picco L, Delai F, Lenzi MA. 2014. Channel Adjustments and Island Dynamics in the Brenta River (Italy) Over the Last 30 Years. River Research and Applications **30** : 719–732. DOI: 10.1002/rra.2676

Mount N, Louis J. 2005. Estimation and propagation of error in measurements of river channel movement from aerial imagery. Earth Surface Processes and Landforms **30** : 635–643. DOI: 10.1002/esp.1172

Mount NJ, Louis J, Teeuw RM, Zukowskyj PM, Stott T. 2003. Estimation of error in bankfull width comparisons from temporally sequenced raw and corrected aerial photographs. Geomorphology **56** : 65–77. DOI: 10.1016/S0169-555X(03)00046-1

Nanson GC, Hickin EJ. 1983. Channel migration and incision on the Beatton River. Journal of Hydraulic Engineering **109** : 327–337.

Nardi L, Rinaldi M. 2015. Spatio-temporal patterns of channel changes in response to a major flood event: the case of the Magra River (central–northern Italy). Earth Surface Processes and Landforms **40** : 326–339. DOI: 10.1002/esp.3636

Necsoiu M, Dinwiddie CL, Walter GR, Larsen A, Stothoff SA. 2013. Multi-temporal image analysis of historical aerial photographs and recent satellite imagery reveals evolution of water body surface area and polygonal terrain morphology in Kobuk Valley National Park, Alaska. Environmental Research Letters **8** : 025007. DOI: 10.1088/1748-9326/8/2/025007

Nelson NC, Erwin SO, Schmidt JC. 2013. Spatial and temporal patterns in channel change on the Snake River downstream from Jackson Lake dam, Wyoming. Geomorphology **200** : 132–142. DOI: 10.1016/j.geomorph.2013.03.019

Nilsson C, Reidy CA, Dynesius M, Revenga C. 2005. Fragmentation and Flow Regulation of the World's Large River Systems. Science **308** : 405–408. DOI: 10.1126/science.1107887

Pizzuto JE. 1994. Channel adjustments to changing discharges, Powder River, Montana. GSA Bulletin **106** : 1494–1501. DOI: 10.1130/0016-7606(1994)106<1494:CATCDP>2.3.CO;2

Rhoades EL, O'Neal MA, Pizzuto JE. 2009. Quantifying bank erosion on the South River from 1937 to 2005, and its importance in assessing Hg contamination. Applied Geography **29** : 125–134. DOI: 10.1016/j.apgeog.2008.08.005

Righini M, Surian N, Wohl E, Marchi L, Comiti F, Amponsah W, Borga M. 2017. Geomorphic response to an extreme flood in two Mediterranean rivers (northeastern Sardinia, Italy): Analysis of controlling factors. Geomorphology **290** : 184–199. DOI: 10.1016/j.geomorph.2017.04.014

Riquelme A, Del Soldato M, Tomás R, Cano M, Jordá Bordehore L, Moretti S. 2019. Digital landform reconstruction using old and recent open access digital aerial photos. Geomorphology **329** : 206–223. DOI: 10.1016/j.geomorph.2019.01.003

Schmidt JC, Wilcock PR. 2008. Metrics for assessing the downstream effects of dams. Water Resources Research **44** : W04404. DOI: 10.1029/2006WR005092

Schook DM, Rathburn SL, Friedman JM, Wolf JM. 2017. A 184-year record of river meander migration from tree rings, aerial imagery, and cross sections. Geomorphology **293** : 227–239. DOI: 10.1016/j.geomorph.2017.06.001

Surian N. 1999. Channel changes due to river regulation: the case of the Piave River, Italy. Earth Surface Processes and Landforms **24** : 1135–1151. DOI: 10.1002/(SICI)1096-9837(199911)24:12<1135::AID-ESP40>3.0.CO;2-F

Surian N, Mao L, Giacomin M, Ziliani L. 2009. Morphological effects of different channel-forming discharges in a gravel-bed river. Earth Surface Processes and Landforms **34** : 1093–1107. DOI: 10.1002/esp.1798

Swanson BJ, Meyer GA, Coonrod JE. 2011. Historical channel narrowing along the Rio Grande near Albuquerque, New Mexico in response to peak discharge reductions and engineering: magnitude and uncertainty of change from air photo measurements. Earth Surface Processes and Landforms **36** : 885–900. DOI: 10.1002/esp.2119

Thompson C, Croke J. 2013. Geomorphic effects, flood power, and channel competence of a catastrophic flood in confined and unconfined reaches of the upper Lockyer valley, southeast Queensland, Australia. Geomorphology **197** : 156–169. DOI: 10.1016/j.geomorph.2013.05.006

Topping DJ, Mueller ER, Schmidt JC, Griffiths RE, Dean DJ, Grams PE. 2018. Long-Term Evolution of Sand Transport Through a River Network: Relative Influences of a Dam Versus Natural Changes in Grain Size From Sand Waves. Journal of Geophysical Research: Earth Surface **123** : 1879–1909. DOI: 10.1029/2017JF004534

Urban MA, Rhoads BL. 2003. Catastrophic human-induced change in stream-channel planform and geometry in an agricultural watershed, Illinois, USA. Annals of the Association of American Geographers **93** : 783–796. DOI: 10.1111/j.1467-8306.2003.09304001.x

USGS. 2012. United States Geological Survey National Elevation Dataset [online] Available from: https://www.usgs.gov/core-science-systems/national-geospatial-program/national-map

USGS. 2019. United States Geological Survey Earth Explorer [online] Available from: https://earthexplorer.usgs.gov/

Wellmeyer JL, Slattery MC, Phillips JD. 2005. Quantifying downstream impacts of impoundment on flow regime and channel planform, lower Trinity River, Texas. Geomorphology **69** : 1–13. DOI: 10.1016/j.geomorph.2004.09.034

Werbylo KL, Farnsworth JM, Baasch DM, Farrell PD. 2017. Investigating the accuracy of photointerpreted unvegetated channel widths in a braided river system: a Platte River case study. Geomorphology **278** : 163–170. DOI: 10.1016/j.geomorph.2016.11.003

Wheaton JM, Brasington J, Darby SE, Sear DA. 2010. Accounting for uncertainty in DEMs from repeat topographic surveys: improved sediment budgets. Earth Surface Processes and Landforms **35** : 136–156. DOI: 10.1002/esp.1886

White JQ, Pasternack GB, Moir HJ. 2010. Valley width variation influences riffle–pool location and persistence on a rapidly incising gravel-bed river. Geomorphology **121** : 206–221. DOI: 10.1016/j.geomorph.2010.04.012

Winterbottom SJ, Gilvear DJ. 1997. Quantification of channel bed morphology in gravel-bed rivers using airborne multispectral imagery and aerial photography. Regulated Rivers: Research & Management **13** : 489–499. DOI: 10.1002/(SICI)1099-1646(199711/12)13:6<489::AID-RRR471>3.0.CO;2-X

Winterbottom SJ, Gilvear DJ. 2000. A GIS-based approach to mapping probabilities of river bank erosion: regulated River Tummel, Scotland. Regulated Rivers: Research & Management: An International Journal Devoted to River Research and Management **16** : 127–140. DOI: 10.1002/(SICI)1099-1646(200003/04)16:2<127::AID-RRR573>3.0.CO;2-Q

Ziliani L, Surian N. 2012. Evolutionary trajectory of channel morphology and controlling factors in a large gravel-bed river. Geomorphology **173–174** : 104–117. DOI: 10.1016/j.geomorph.2012.06.001

Table and figure captions:

Table 1: Uncertainty bounds for the ε_1 and ε_2 methods and the 95% credible intervals for the SDP method. All values are normalized by the channel centerline length. Also included are the percent change between the ε_1 and SDP method ($\%\Delta SDP_{\varepsilon 1}$) and between the ε_2 and SDP method ($\%\Delta SDP_{\varepsilon 2}$).

Figure 1: SDP algorithm flow chart.

Figure 2: Spatially distributed image co-registration error surface. (A) Image co-registration error in the X direction (ε_x). (B) Image co-registration error in the Y direction (ε_y). Positive ε_x and ε_y values point east and north, respectively. ε_x and ε_y were calculated by equations 3 and 4. (C) Resultant vectors of ε_x and ε_y calculated by equations 5 and 6.

Figure 3: Schematic showing minimum and maximum active channel delineations for interpretation uncertainty. (A) Minimum and maximum extent of the active channel and vegetated islands. These extents represent uncertainty in interpreting the channel and vegetated island boundaries. (B) Maximum area of the active channel (A_{max}) is the minimum extent of the vegetated islands subtracted from the maximum extent of the active channel. (C) Minimum area of the active channel (A_{min}) is the maximum extent of the vegetated islands subtracted from the minimum extent of the active channel.

Figure 4: Steps used to create a probabilistic boundary delineation. (A) Original boundary delineation in green and boundary delineation adjusted for co-registration error in red. The red line was created by moving each vertex of the green line by a distance of $\|\underset{\varepsilon_{xy}}{\rightarrow}\|$ in the direction θ (Figure 1c). (B) Subset of A. Blue lines represent the distribution of probable channel delineations around the adjusted red boundary. The distribution of blue lines was populated by randomly sampling a digitizing uncertainty from a normal distribution with a mean (μ) of zero and standard deviation (σ) of one-third the maximum digitizing uncertainty (inset). Each vertex on the red line was moved along a normal vector with a magnitude equal to the sampled value. This was repeated 100 times. (C) Same location as B showing the full probabilistic boundary delineation. Each red line was adjusted from the original green boundary using one of the 10 co-registration error surfaces. The blue lines represent the digitization uncertainty around each of the 10 red lines.

Figure 5: Study area used to illustrate the SDP method. The study area is located in northwestern Colorado along a 17 km alluvial section of the Yampa River spanning the Little Snake confluence and a 7 km reach of the Little Snake River directly upstream from the confluence. The Deerlodge gage (USGS station #: 09260050) is located at the downstream end of the study area. The direction of flow is from right to left. Base aerial image is from the 2017 NAIP.

Figure 6: Interpretation uncertainty characterized by minimum and maximum channel boundary delineations. (A) Partly vegetated surface on the left bank was classified as a vegetated island and a secondary channel using the A_{max} delineation. (B) Same vegetated surface as A was classified as floodplain in the A_{min} delineation. (C) Vegetated bank-attached bar on the right bank was classified as active channel in the A_{max} delineation. (D) Same bank-attached bar as C was classified as floodplain in the A_{min} delineation. Direction of flow is from top to bottom in all images and minimum and maximum boundaries were delineated from the 1954 aerial image.

Figure 7: Minimum and maximum extent of erosion and deposition was calculated by adding or subtracting a spatially uniform uncertainty bound around each polygon of erosion and deposition. Flow is from right to left and the 1954 image was used as the base image. The maximum area of erosion or deposition is the uncertainty bound added to each polygon (A, B, C) and the minimum area of erosion or deposition is the uncertainty bound subtracted from each polygon (D, E, F). The minimum bound of net planform change was the sum of erosional polygons in C subtracted from the sum of depositional polygons in F, and the maximum bound of net planform change was the sum of erosional polygons in F subtracted from the sum of depositional polygons in C.

Figure 8: Minimum and maximum extent of erosion and deposition using the $A_{max(t1)}$&$A_{max(t2)}$ overlay. Flow is from right to left and the 1954 image was used as the base image. (A) Maximum extent of deposition and erosion using the ε_1 method. (B) Minimum extent of deposition and erosion using the ε_1 method. (C) Maximum extent of erosion and deposition using the SDP method. Inset shows the estimate for the normalized area of deposition and minimum and maximum bound of uncertainty using the ε_1 and ε_2 methods overlaid on the SDP distribution. (D) Minimum extent of erosion and deposition using the SDP method. Inset shows the estimate for the normalized area of erosion and minimum and maximum bound of uncertainty using the ε_1 and ε_2 methods overlaid on the SDP distribution. The maximum and minimum extent of erosion and deposition using the ε_2 method was not overlaid on the images because the ε_2 method calculated the magnitude of uncertainty, not the spatial extent. The SDP method reduced the magnitude of uncertainty by 72-78% for deposition and 84-87% for erosion (Table 1).

Figure 9: (A) All A_{max} and A_{min} overlay solutions merged into a single histogram fit with a probability density function which represents uncertainty in the normalized net change in area caused by co-registration, digitization, and interpretation uncertainty. The minimum and maximum bounds of uncertainty for the ε_1 and ε_2 methods are also shown. (B) Net areal change in A for changes that occurred along the channel margin. (C) Net areal change in A for changes that occurred along vegetated islands.

Figure 10: Box and whisker plot for each error and uncertainty type showing the median and interquartile range within the box, values ±2.7σ within the whiskers, and values < ±2.7σ as outliers.

Figure 11: Net planform change using each A_{min} and A_{max} overlay. Each panel shows the estimate for the normalized net change in area, the minimum and maximum bound of uncertainty using the ε_1 and ε_2 methods, and a histogram of the SDP solutions fit with a probability density function. (A) $A_{max(t1)}$&$A_{min(t2)}$ overlay. (B) $A_{min(t1)}$&$A_{max(t2)}$ overlay. (C) $A_{max(t1)}$&$A_{max(t2)}$ overlay. (D) $A_{min(t1)}$&$A_{min(t2)}$ overlay.

Figure 12: Probability density functions fit to the A_{min} and A_{max} overlay distributions partitioned by change along the channel margins and vegetated islands. (A) Normalized area of deposition along the channel margins. (B) Normalized net change along the channel margins.

Figure 13: Violin plots showing the distribution of net planform change calculated by the SDP method using 1,000 to 10,000 randomly sampled channel boundary delineations indicated by the number of bootstrap iterations. Insets show the mean and standard deviation for each violin plot.

Figure 14: Example of the ε_1 and ε_2 methods and SDP method applied to two locations of bank retreat in our study area. (A) Location of small bank retreat. (B) Magnitude of channel change at the site in A calculated by the ε_1 and ε_2 methods and SDP method. (C) Location of large bank retreat. (D) Magnitude of channel change at the site in C calculated by the ε_1 and ε_2 methods and SDP method.

Figure 15: Distribution of co-registration errors extracted from each vertex along the A_{max} and A_{min} boundaries in 1954 and 1961. These data are displayed as a cumulative density function estimate and a histogram. The blue portion of these distributions have a co-registration error that is lower than the uniform RMSE and the green portion have a co-registration error that is above the uniform RMSE. 82% of the co-registration errors were above the uniform RMSE in 1954 and 84% in 1961.

	$\mathcal{E}_1$ (m)	$\mathcal{E}_2$ (m)	SDP (m)	%ΔSDP$_{\varepsilon1}$	%ΔSDP$_{\varepsilon2}$
Deposition					
$A_{Max(t1)}$&$A_{Min(t2)}$	2.6 – 26.9	-7.6 – 20.5	8.4 – 11.2	89%	90%
$A_{Min(t1)}$&$A_{Max(t2)}$	0.6 – 20.5	-3.7 – 20.7	4.12 – 6.7	87%	89%
$A_{Max(t1)}$&$A_{Max(t2)}$	1.1 – 23.1	-6.2 – 20.0	5.5 – 8.1	88%	90%
$A_{Min(t1)}$&$A_{Min(t2)}$	1.3 – 23.4	-6.3 – 19.9	5.9 - 8.7	87%	89%
TOTAL	0.6 – 23.4	-7.6 – 20.7	4.4 – 10.6	72%	78%
Erosion					
$A_{Max(t1)}$&$A_{Min(t2)}$	0.4 – 26.4	-10.5 – 23.4	5.6 – 9.6	85%	88%
$A_{Min(t1)}$&$A_{Max(t2)}$	0.9 - 31.2	-10.3 – 27.3	7.5 – 11.6	86%	89%
$A_{Max(t1)}$&$A_{Max(t2)}$	0.4 – 28.8	-11.6 – 25.4	6.1 – 10.1	86%	89%
$A_{Min(t1)}$&$A_{Min(t2)}$	0.4 – 27.5	-10.6 – 24.2	5.8 – 10.0	85%	88%
TOTAL	0.4 – 31.2	-11.6 – 27.3	5.92 – 10.8	84%	87%
Δ Planform Change					
$A_{Max(t1)}$&$A_{Min(t2)}$	-23.8 – 26.6	-28.7 – 13.8	-1.1 - 5.5	87%	84%
$A_{Min(t1)}$&$A_{Max(t2)}$	-30.5 – 19.6	-35.2 – 7.6	-7.4 – 0.8	87%	84%
$A_{Max(t1)}$&$A_{Max(t2)}$	-27.8 – 22.7	-32.9 – 9.4	-4.6 – 1.9	87%	85%
$A_{Min(t1)}$&$A_{Min(t2)}$	-26.2 – 23.0	-31.1 – 10.0	-4.1 – 2.8	83%	83%
TOTAL	-27.4 – 26.6	-35.2 – 13.8	-6.3 – 4.5	80%	78%

Table 1

Figure 1

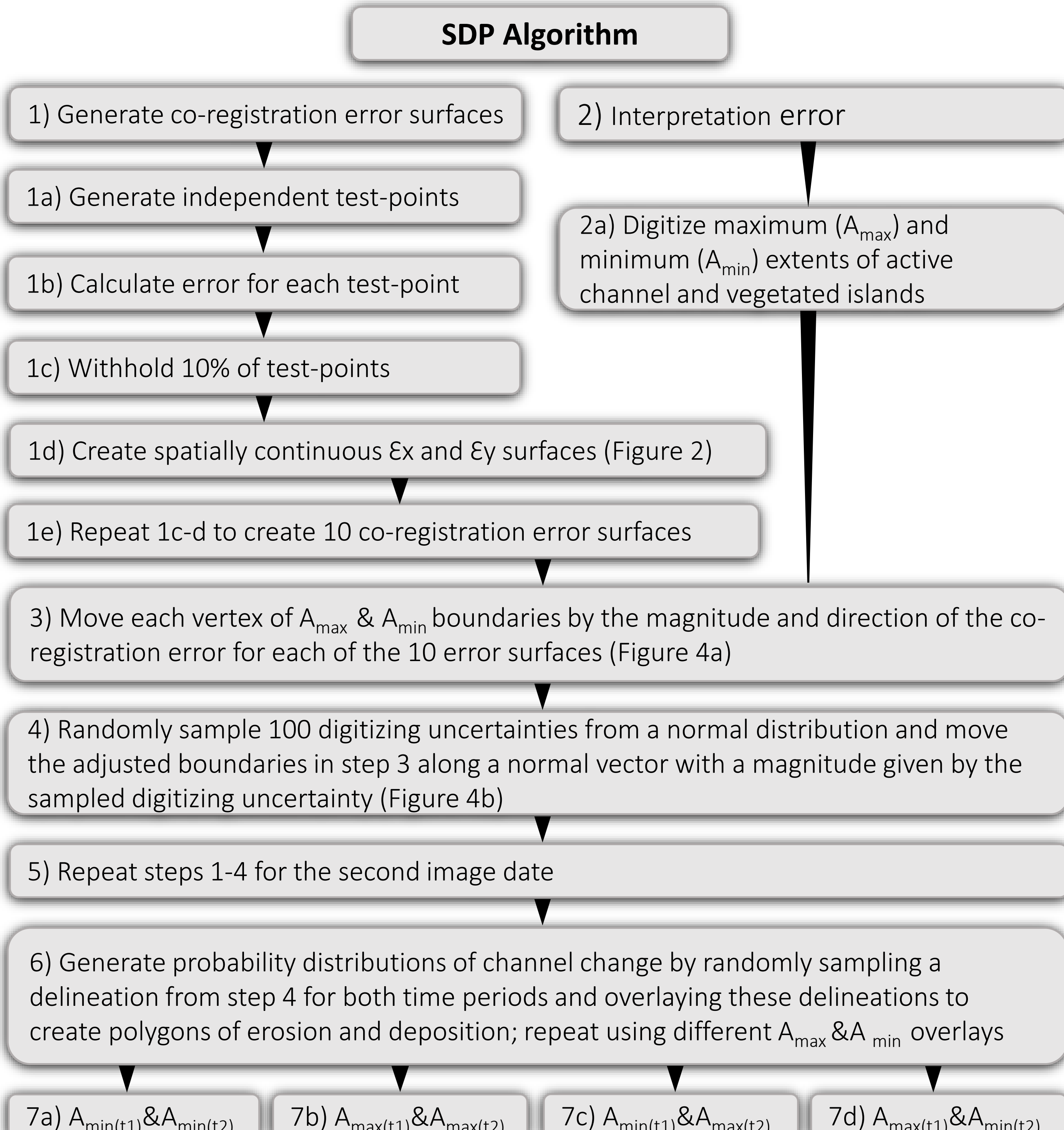
SDP Algorithm
1) Generate co-registration error surfaces
1a) Generate independent test-points
1b) Calculate error for each test-point
1c) Withhold 10% of test-points
1d) Create spatially continuous Ɛx and Ɛy surfaces (Figure 2)
1e) Repeat 1c-d to create 10 co-registration error surfaces
2) Interpretation error
2a) Digitize maximum (A_{max}) and minimum (A_{min}) extents of active channel and vegetated islands
3) Move each vertex of A_{max} & A_{min} boundaries by the magnitude and direction of the co-registration error for each of the 10 error surfaces (Figure 4a)
4) Randomly sample 100 digitizing uncertainties from a normal distribution and move the adjusted boundaries in step 3 along a normal vector with a magnitude given by the sampled digitizing uncertainty (Figure 4b)
5) Repeat steps 1-4 for the second image date
6) Generate probability distributions of channel change by randomly sampling a delineation from step 4 for both time periods and overlaying these delineations to create polygons of erosion and deposition; repeat using different A_{max} &A_{min} overlays
7a) $A_{min(t1)}$&$A_{min(t2)}$
7b) $A_{max(t1)}$&$A_{max(t2)}$
7c) $A_{min(t1)}$&$A_{max(t2)}$
7d) $A_{max(t1)}$&$A_{min(t2)}$

Figure 2

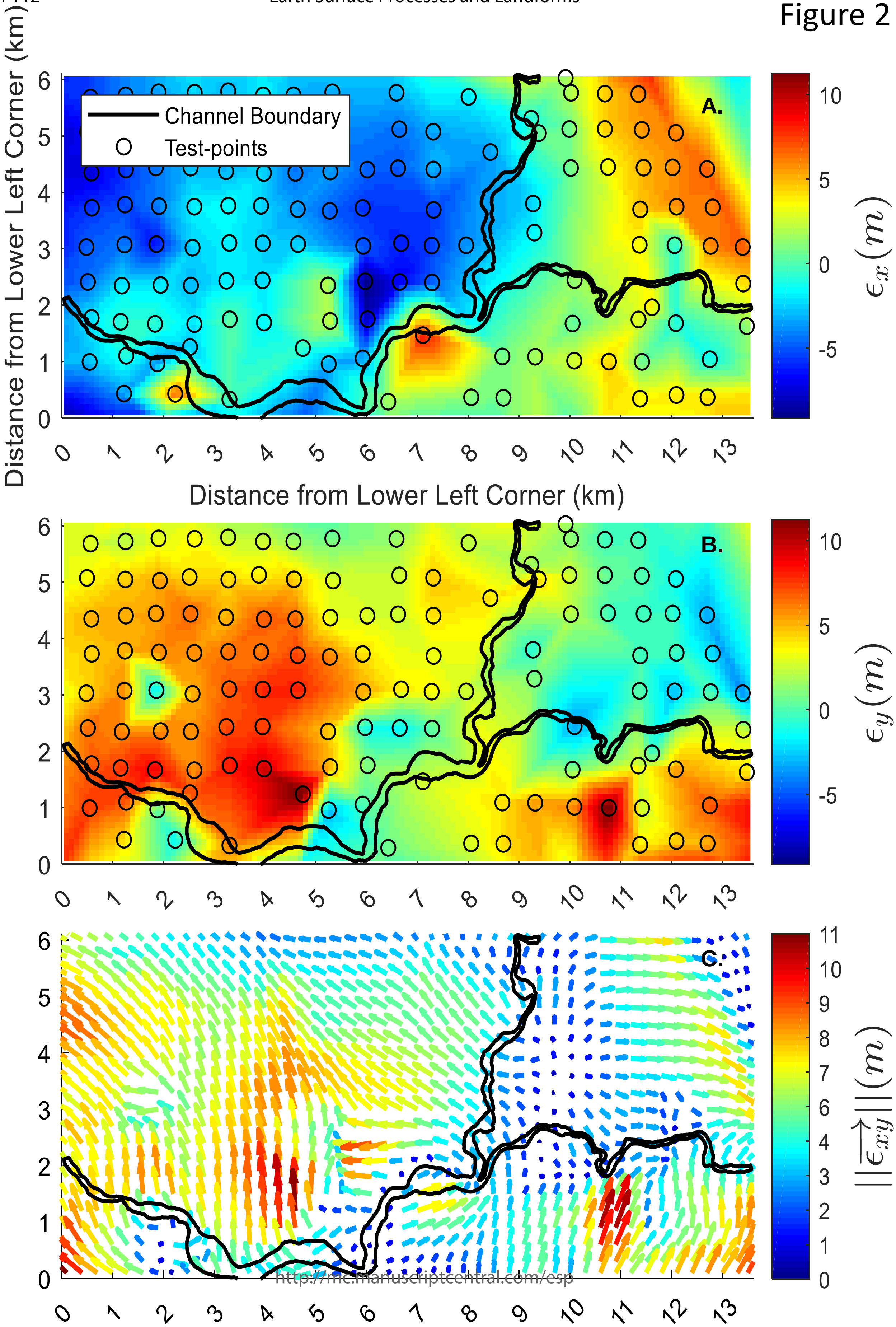
A.
Channel Boundary
Test-points
Distance from Lower Left Corner (km)
Distance from Lower Left Corner (km)
$\epsilon_x(m)$
B.
$\epsilon_y(m)$
C.
$||\overrightarrow{\epsilon_{xy}}||(m)$

Figure 3

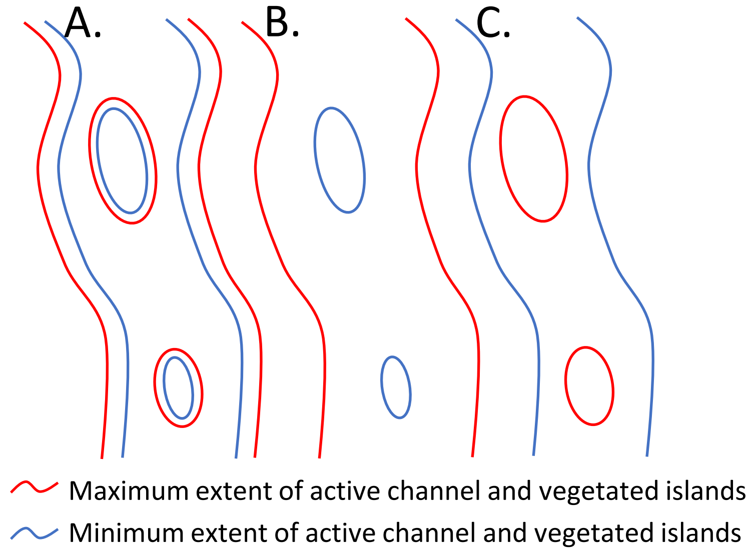
A.
B.
C.
Maximum extent of active channel and vegetated islands
Minimum extent of active channel and vegetated islands

Figure 4

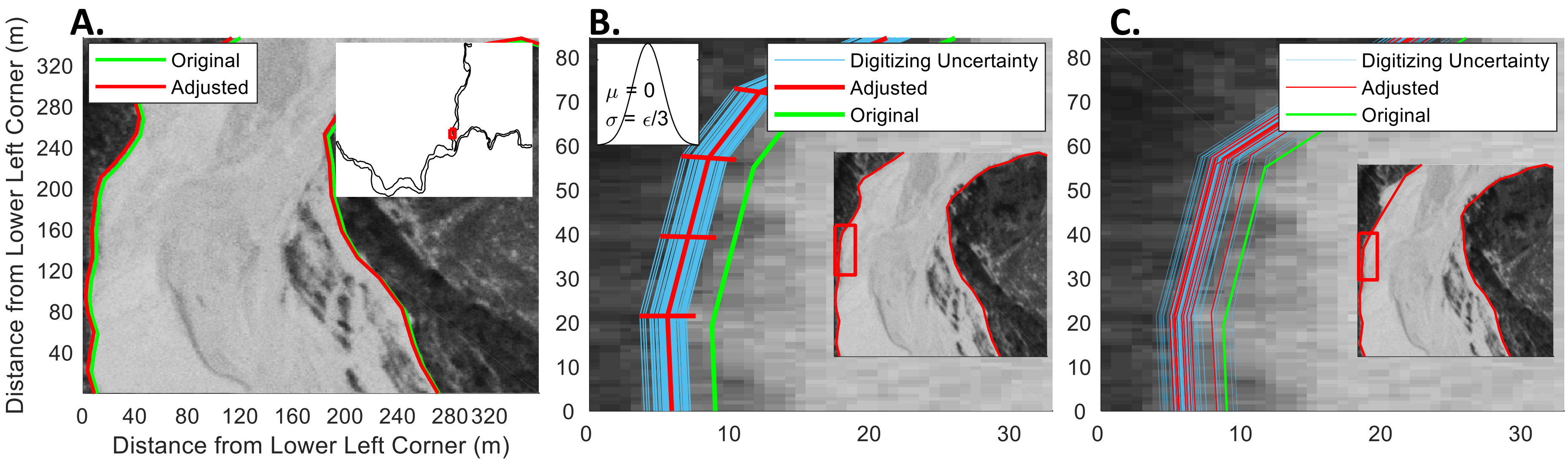
A.
Original
Adjusted
Distance from Lower Left Corner (m)
Distance from Lower Left Corner (m)
0
40
80
120
160
200
240
280
320
B.
$\mu = 0$
$\sigma = \epsilon/3$
Digitizing Uncertainty
Adjusted
Original
0
10
20
30
40
50
60
70
80
C.
Digitizing Uncertainty
Adjusted
Original

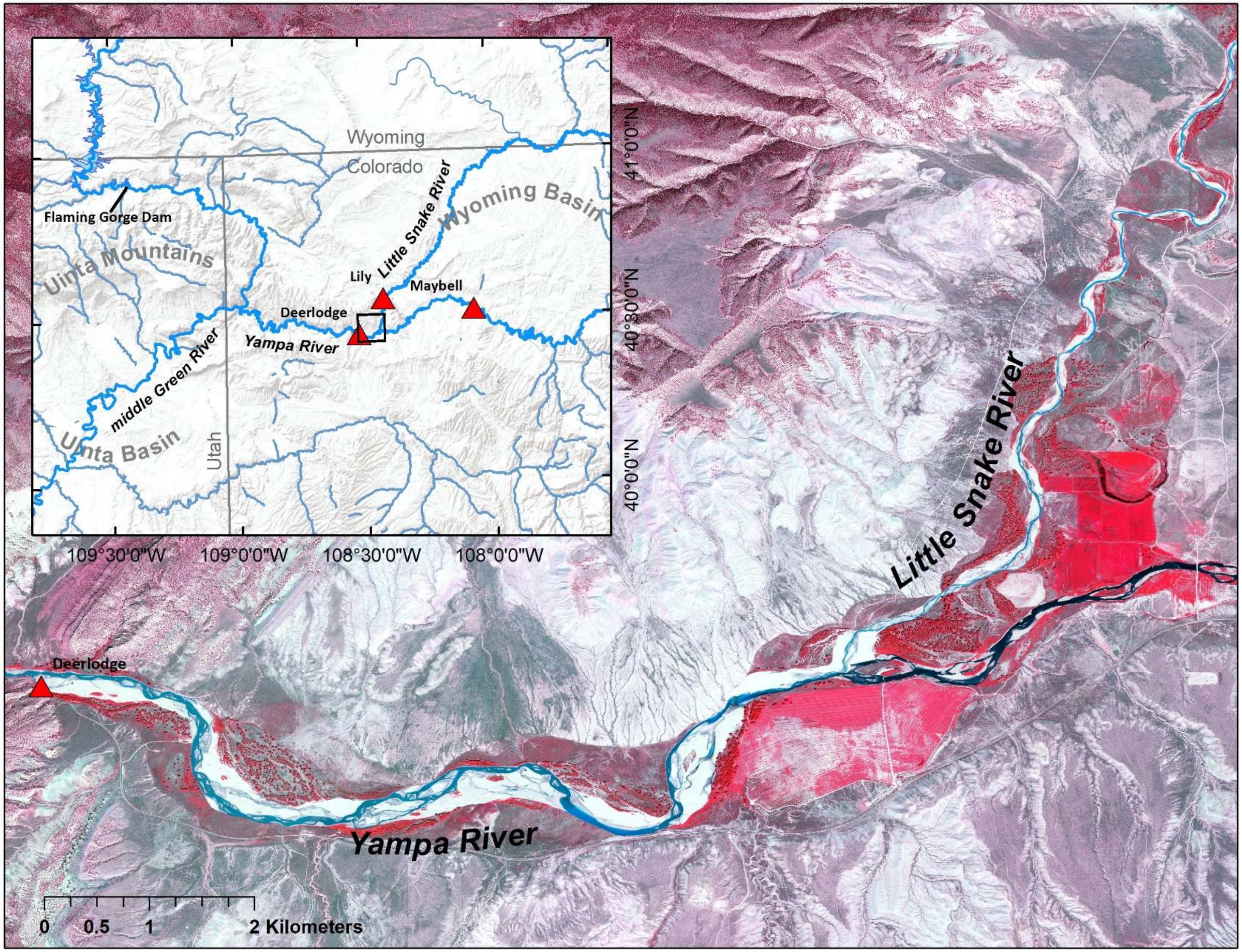
Wyoming
Colorado
Flaming Gorge Dam
Uinta Mountains
Wyoming Basin
Little Snake River
Lily
Maybell
Deerlodge
Yampa River
middle Green River
Uinta Basin
Utah
41°0'0"N
40°30'0"N
40°0'0"N
109°30'0"W
109°0'0"W
108°30'0"W
108°0'0"W
Deerlodge
Little Snake River
Yampa River
0 0.5 1 2 Kilometers

Figure 6

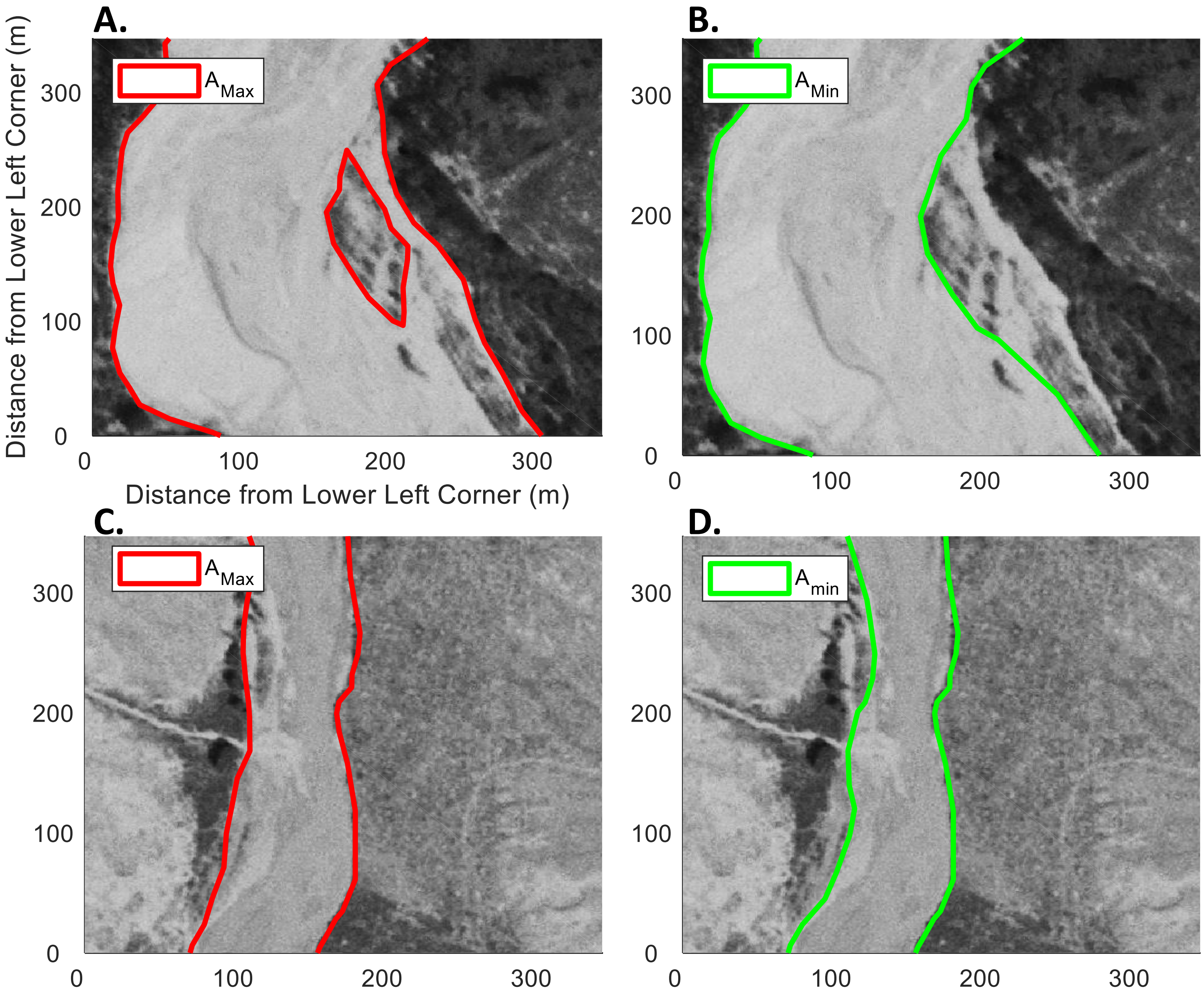
A.
B.
C.
D.
A Max
A Min
A Max
A min
Distance from Lower Left Corner (m)
Distance from Lower Left Corner (m)
0
100
200
300

Figure 7

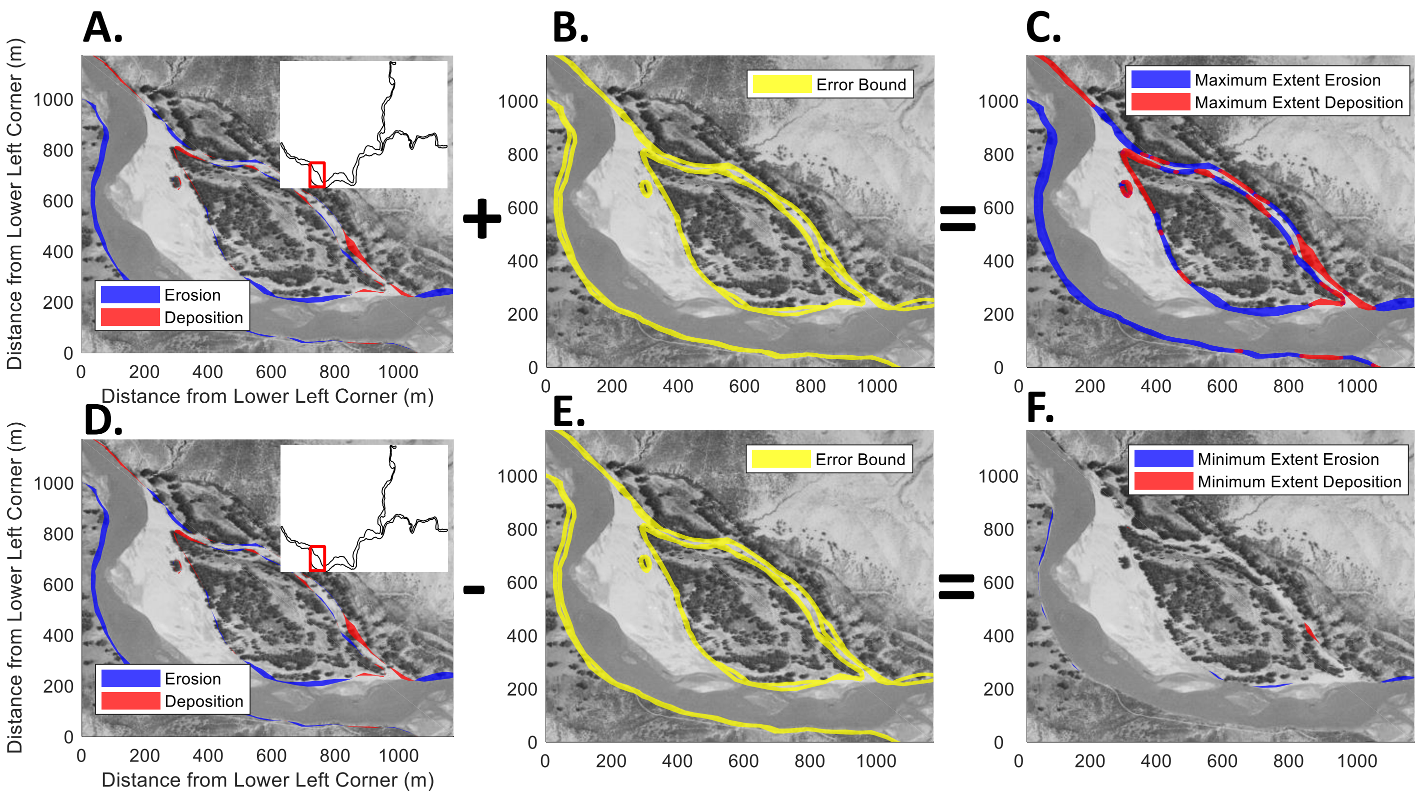
A.
B.
C.
D.
E.
F.
+
=
-
=
Erosion
Deposition
Error Bound
Maximum Extent Erosion
Maximum Extent Deposition
Minimum Extent Erosion
Minimum Extent Deposition
Distance from Lower Left Corner (m)
Distance from Lower Left Corner (m)
0
200
400
600
800
1000

Figure 8

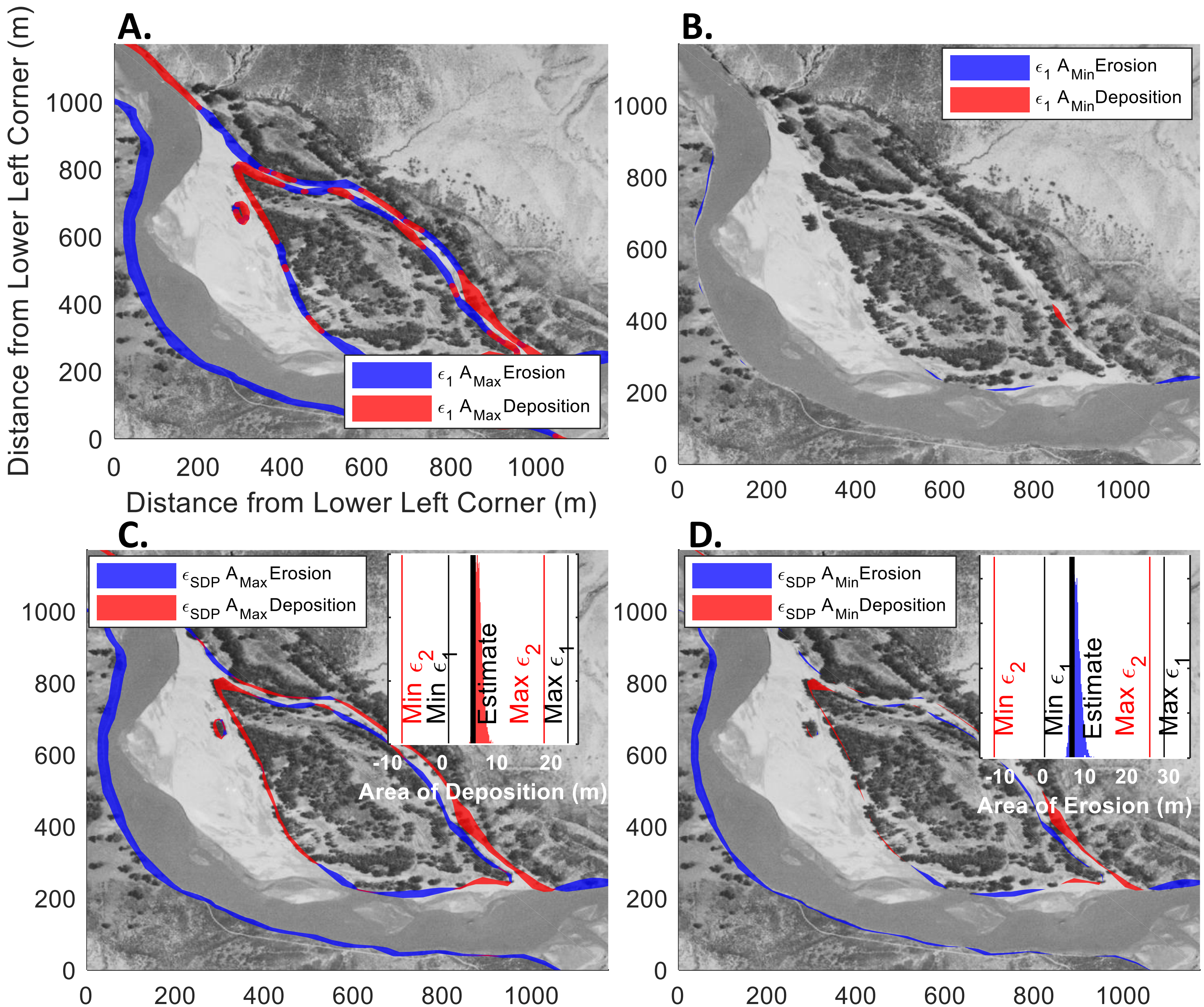
A.
B.
C.
D.
Distance from Lower Left Corner (m)
Distance from Lower Left Corner (m)
ϵ1 AMax Erosion
ϵ1 AMax Deposition
ϵ1 AMin Erosion
ϵ1 AMin Deposition
ϵSDP AMax Erosion
ϵSDP AMax Deposition
ϵSDP AMin Erosion
ϵSDP AMin Deposition
Min ϵ2
Min ϵ1
Estimate
Max ϵ2
Max ϵ1
Area of Deposition (m)
Area of Erosion (m)
0
200
400
600
800
1000
-10
10
20
30

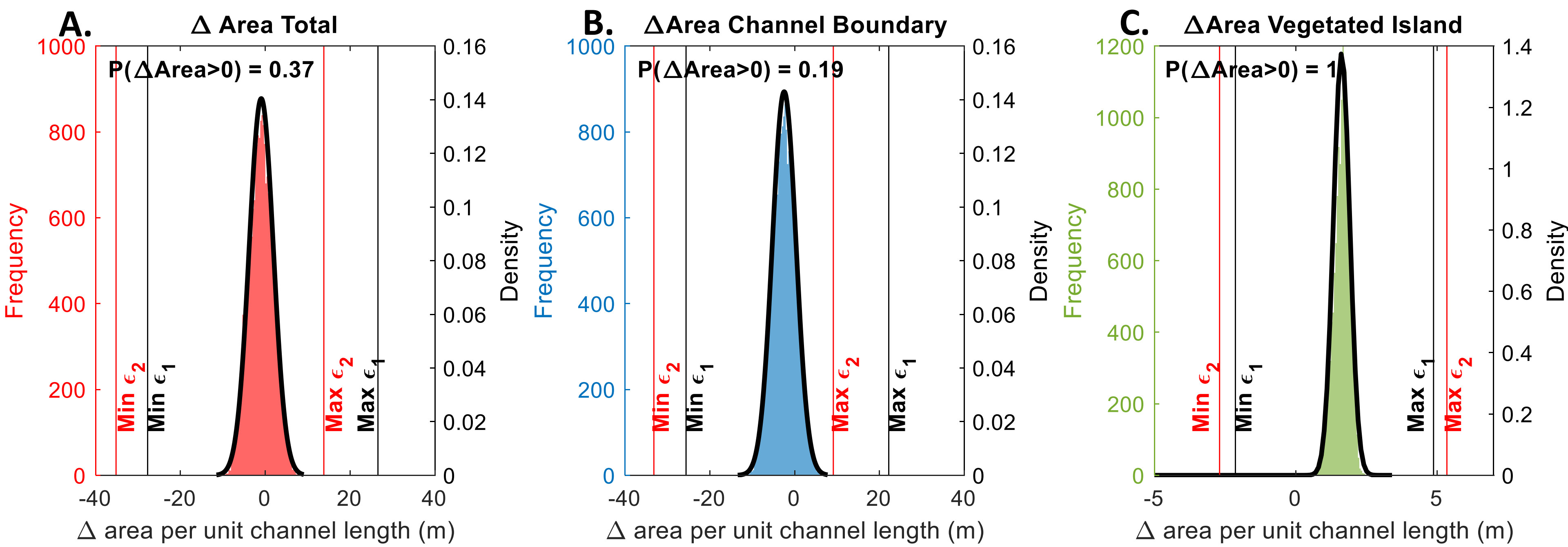
A.
Δ Area Total
P(ΔArea>0) = 0.37
Frequency
Density
Min ϵ2
Min ϵ1
Max ϵ2
Max ϵ1
Δ area per unit channel length (m)
B.
ΔArea Channel Boundary
P(ΔArea>0) = 0.19
Frequency
Density
Min ϵ2
Min ϵ1
Max ϵ2
Max ϵ1
Δ area per unit channel length (m)
C.
ΔArea Vegetated Island
P(ΔArea>0) = 1
Frequency
Density
Min ϵ2
Min ϵ1
Max ϵ1
Max ϵ2
Δ area per unit channel length (m)

Figure 10

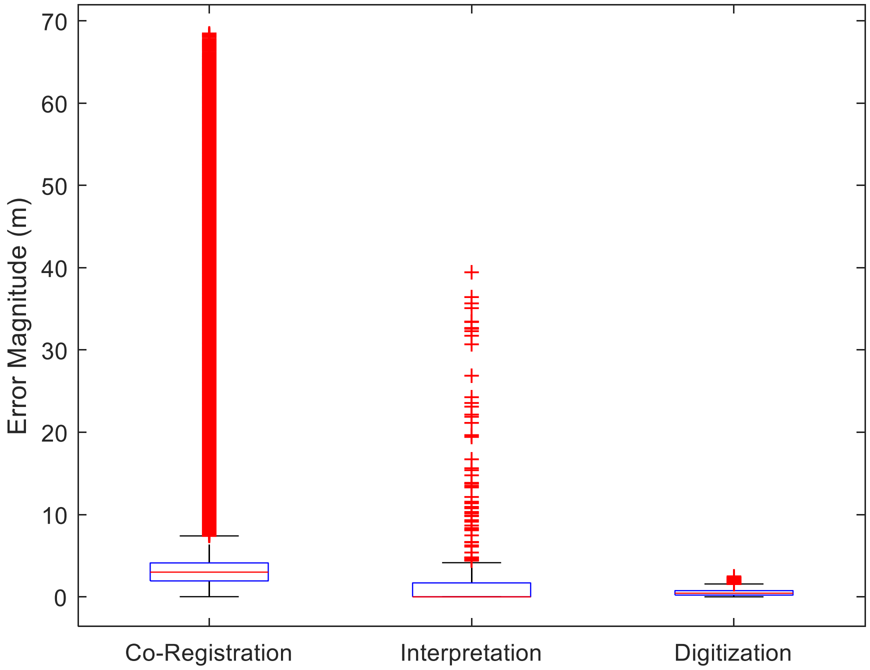
70
60
50
40
30
20
10
0
Error Magnitude (m)
Co-Registration
Interpretation
Digitization

Figure 11

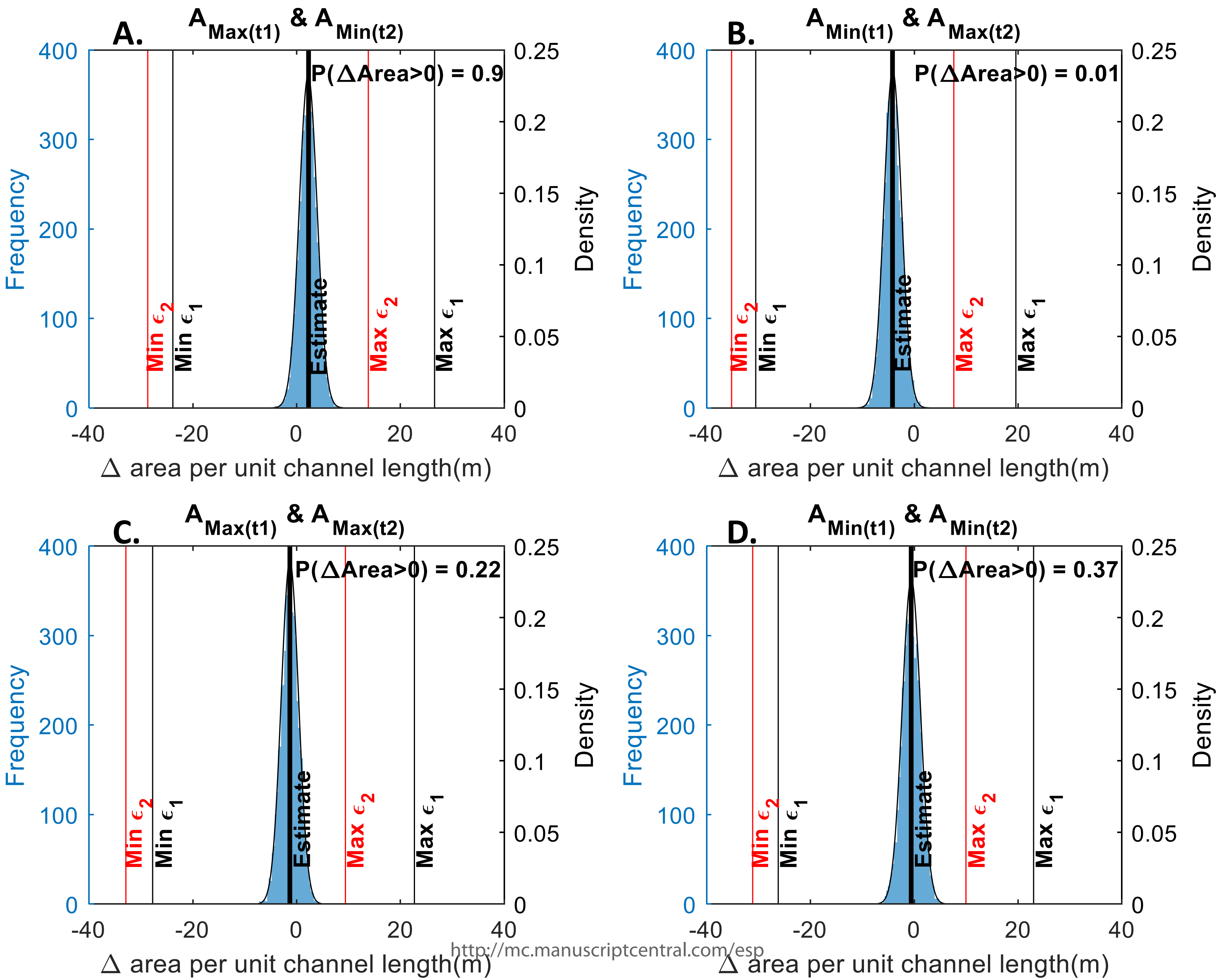
A.
$A_{Max(t1)}$ & $A_{Min(t2)}$
P(ΔArea>0) = 0.9
B.
$A_{Min(t1)}$ & $A_{Max(t2)}$
P(ΔArea>0) = 0.01
C.
$A_{Max(t1)}$ & $A_{Max(t2)}$
P(ΔArea>0) = 0.22
D.
$A_{Min(t1)}$ & $A_{Min(t2)}$
P(ΔArea>0) = 0.37
Min ϵ_2
Min ϵ_1
Estimate
Max ϵ_2
Max ϵ_1
Frequency
Density
Δ area per unit channel length(m)

Figure 12

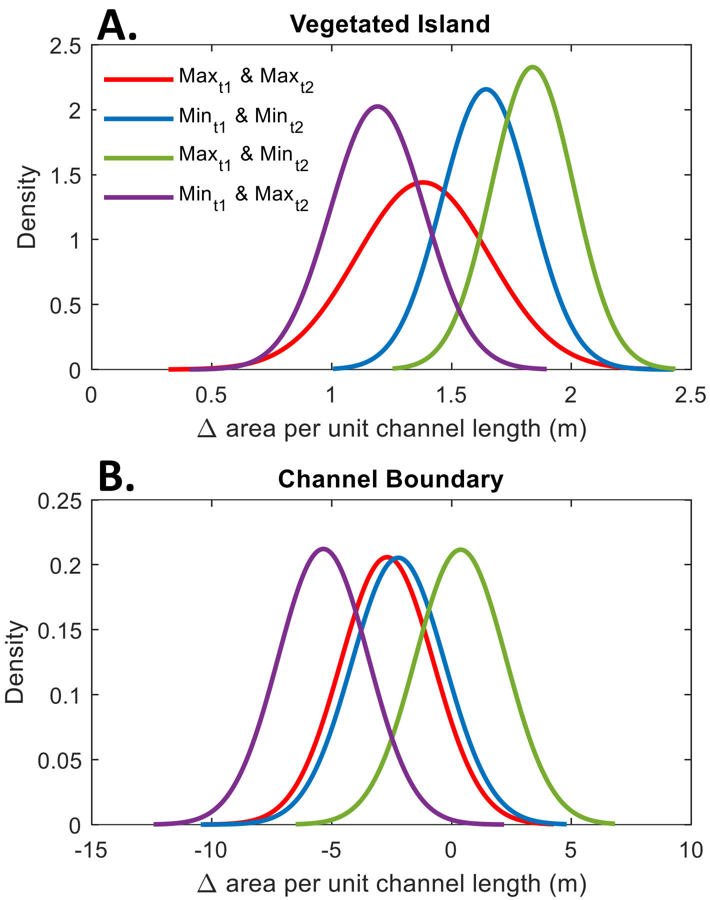
A.
Vegetated Island
Max_t1 & Max_t2
Min_t1 & Min_t2
Max_t1 & Min_t2
Min_t1 & Max_t2
Density
2.5
2
1.5
1
0.5
0
0
0.5
1
1.5
2
2.5
Δ area per unit channel length (m)
B.
Channel Boundary
Density
0.25
0.2
0.15
0.1
0.05
0
-15
-10
-5
0
5
10
Δ area per unit channel length (m)

Figure 13

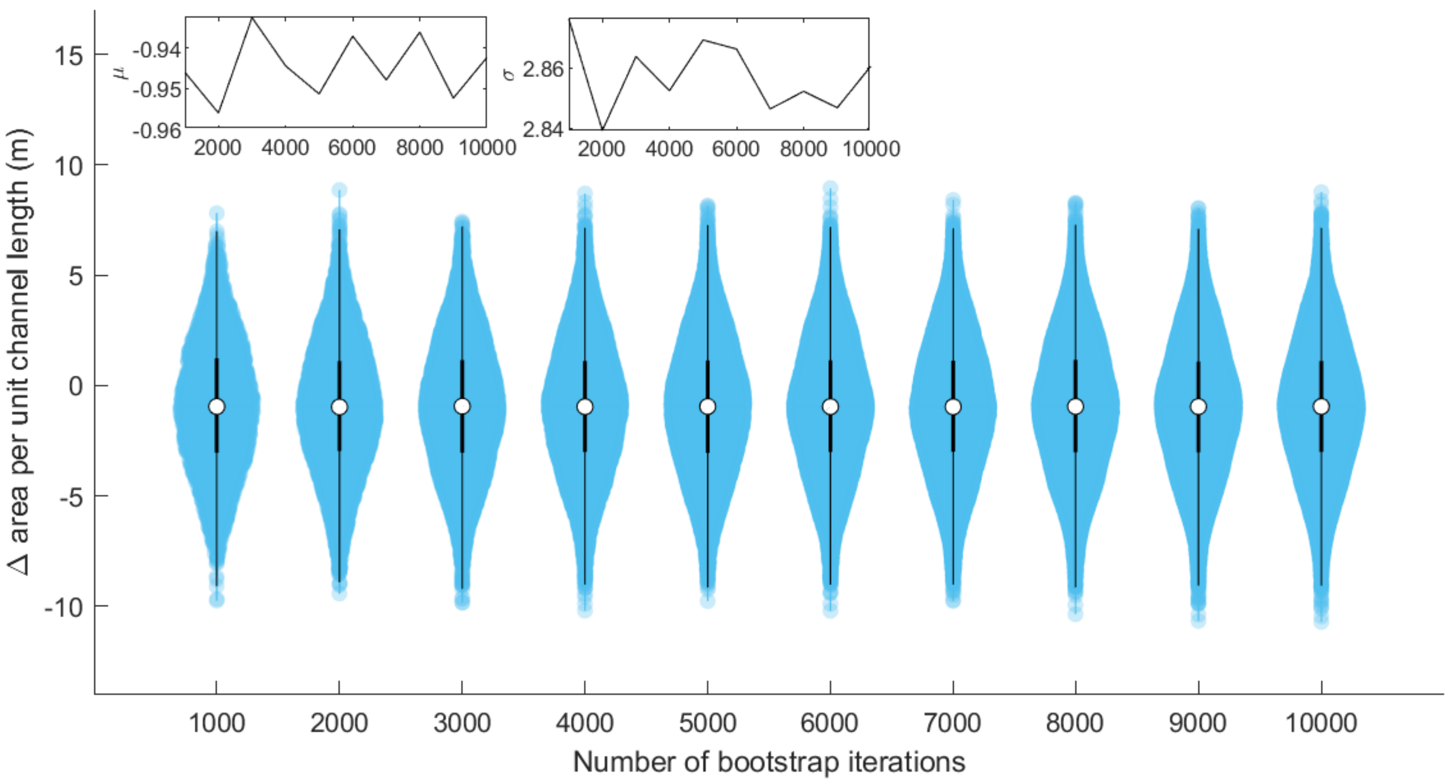
μ
-0.94
-0.95
-0.96
2000
4000
6000
8000
10000
σ
2.86
2.84
2000
4000
6000
8000
10000
15
10
5
0
-5
-10
Δ area per unit channel length (m)
1000
2000
3000
4000
5000
6000
7000
8000
9000
10000
Number of bootstrap iterations

Figure 14

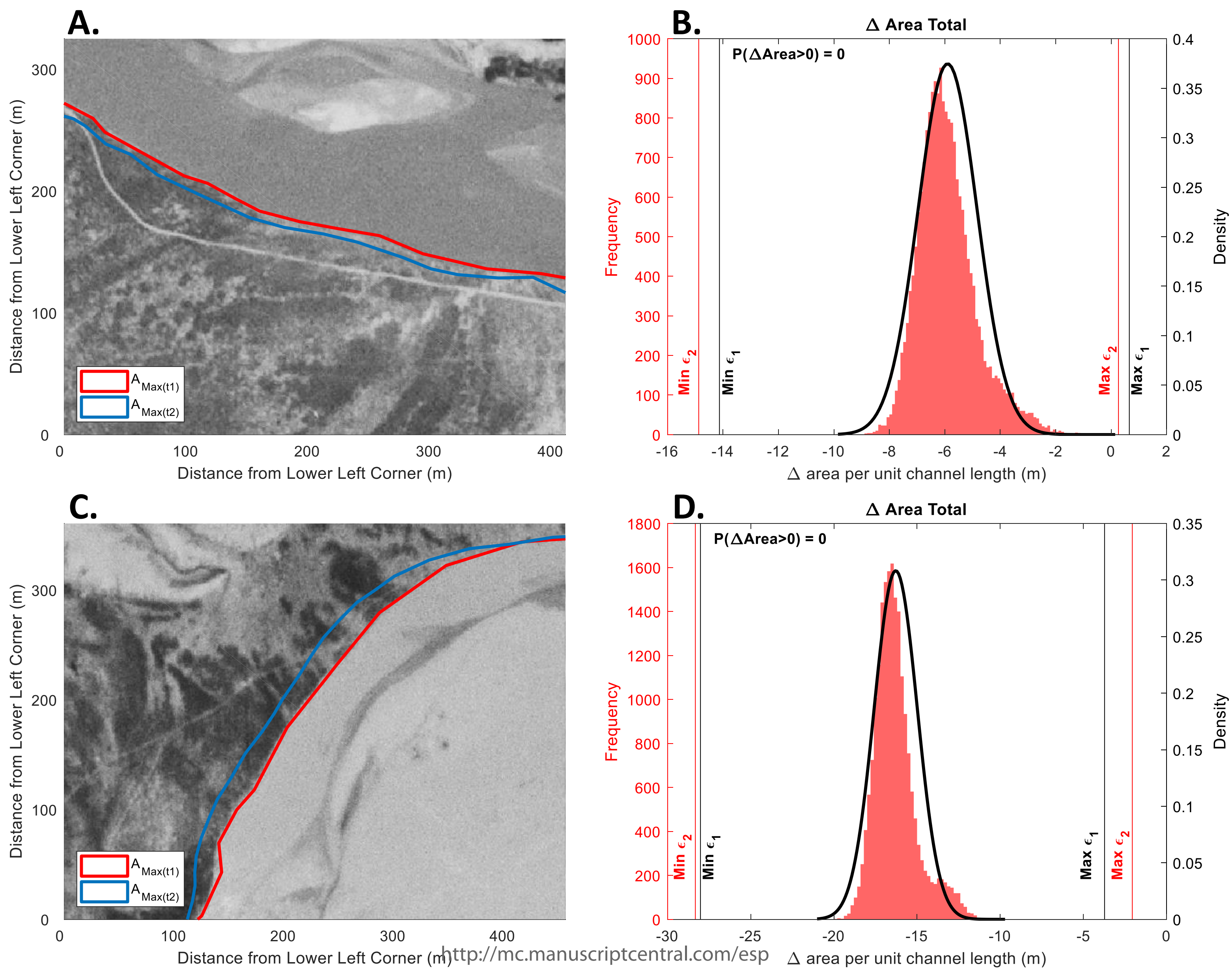
A.
B.
C.
D.
Δ Area Total
P(ΔArea>0) = 0
Distance from Lower Left Corner (m)
Frequency
Density
Δ area per unit channel length (m)
Min ε2
Min ε1
Max ε2
Max ε1
AMax(t1)
AMax(t2)

Figure 15

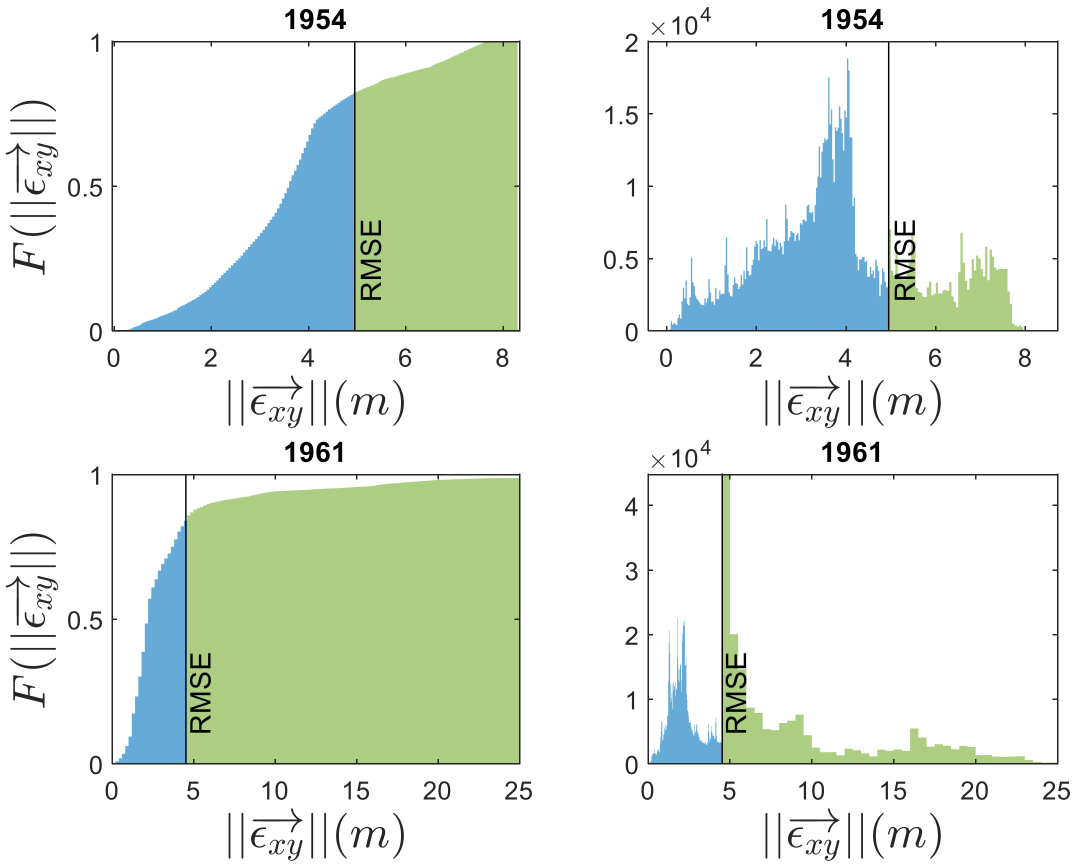
1954
1954
1961
1961
RMSE
RMSE
RMSE
RMSE
$F(||\overrightarrow{\epsilon_{xy}}||)$
$||\overrightarrow{\epsilon_{xy}}||(m)$
$\times 10^4$

Supplemental Information:

Step-by-step instructions for SDP Algorithm

1) *Image Warping*: If the aerial images are not in a real world coordinate system, they must be geo-referenced using image warping. All unregistered images should be warped to the same base image. We refer the reader to Gilvear and Bryant (2003), Mount et al. (2003), and Hughes et al. (2006) for background on image warping.
2) *Image co-registration:* The image co-registration error can be quantified after the images are in the same coordinate system. We define co-registration error as the misalignment between the image being digitized and the most recent image in the time series (Figure 1 step 1).
    a. *Independent test-point:* Identify test-points by extracting the map coordinate of the same feature on the image that is being digitized and the most recent image in the time series (Figure 1 step 1a). Note that the image co-registration error will be zero when the channel boundary is being delineated from the most recent image.
    b. *Magnitude of co-registration error*: The magnitude of each test-point error is calculated in the X and Y directions by subtracting the test-point coordinate in the image being used to delineate the channel boundary (x_i', y_i') from the same test-point coordinate in the most recent image (x_i, y_i) (Figure step 1b):

    $$\varepsilon_{xi} = x_i - x_i' \; ; \quad (3)$$

    $$\varepsilon_{yi} = y_i - y_i' \; ; \quad (4)$$

    where ε_{xi} is the magnitude of co-registration error in the X direction for the i^{th} test point and ε_{yi} is the magnitude of co-registration error in the Y direction for the i^{th} test point. Positive errors in ε_x and ε_y are in the east and north directions.
    c. *Create an ε_x and ε_y surface:* Use bi-linear interpolation between ε_{xi} and ε_{yi} to create a continuous surface of ε_x and ε_y over the entire study area (Figure step 1d).

d. *Calculate the magnitude and direction of co-registration error:* Using the interpolated surface in step 2c, the magnitude $\left(\left\|\overrightarrow{\varepsilon_{xy}}\right\|\right)$ and direction (θ) of co-registration error can be calculated for any coordinate pair (x_j, y_j):

$$\left\|\overrightarrow{\varepsilon_{xy}}\right\| = \left({\varepsilon_{xj}}^2 + {\varepsilon_{yj}}^2\right)^{0.5}; \tag{5}$$

$$\theta = tan^{-1}\left(\frac{\varepsilon_{yj}}{\varepsilon_{xj}}\right); \tag{6}$$

where ε_{xj} and ε_{yj} are the co-registration errors in the X and Y directions at point (x_j, y_j) extracted from the ε_x *and* ε_y surface in step 2c.

e. *Account for the spatial distribution of test-points:* The spatial distribution of test-points will affect the interpolation of ε_x and ε_y. Therefore, repeatedly withhold 10% of the test-points using a 10-fold cross-validation to generate ten ε_x and ε_y surfaces. Using each of the ten interpolated surfaces, repeat steps 2a-d to calculate $\left\|\overrightarrow{\varepsilon_{xy}}\right\|$ *and* θ at any x_j, y_j point (Figure 1 step 1e).

3) *Interpretation uncertainty:* Digitize the maximum and minimum active channel and vegetated island boundaries, thereby accounting for uncertainty in interpretation (Figure 1 step 2).

4) *Calculate* $\left\|\overrightarrow{\varepsilon_{xy}}\right\|$ *and* θ *along the boundary delineation:* Densify the vertices along the A_{max} and A_{min} boundaries from step 3 using an interval that is small enough as to not simplify the A_{max} and A_{min} boundaries (e.g., 1/10 the mean channel width) and calculate $\left\|\overrightarrow{\varepsilon_{xy}}\right\|$ and θ at each vertex using one of the ten ε_x and ε_y surfaces from step 2e.

5) *Adjust each vertex by the co-registration error:* Move each vertex in step 4 by the magnitude of $\left\|\overrightarrow{\varepsilon_{xy}}\right\|$ in the direction of θ. This step creates a new active channel delineation that is adjusted by the co-registration error in one of the 10 ε_x and ε_y surfaces from step 2e (Figure 1 step 3).

6) *Digitization uncertainty:* Digitization uncertainty is estimated probabilistically by randomly sampling 100 values from a normal distribution with a mean of zero and a standard deviation of one third the maximum digitizing uncertainty. The method also includes an option to define the maximum digitizing uncertainty as the number of pixels multiplied by the pixel resolution. For each randomly sampled uncertainty value, the vertices in step 5 are moved along a normal vector with a magnitude given by the uncertainty value (Figure 1 step 4). This process generates 100 delineations of the channel boundary.
7) *Repeat for all co-registration error surfaces:* Repeat steps 4-6 for each co-registration error surface in step 2e. This produces *m X n* delineations for each maximum and minimum active channel boundary, where *m* is the number of error surfaces generated in step 2e and *n* is the number of times that the digitization error is sampled in step 6. In the manuscript example, m is 10 and n is 100, which generates 1000 delineations of the channel boundary. The *m X n* delineations represent a probabilistic boundary delineation for A_{max} and A_{min}.
8) *Create probabilistic boundary delineations for a second aerial image:* Repeat steps 2-7 for a second image that will be compared to the first to quantify channel change (Figure 1 step 5).
9) *Generate probability distributions of channel change:* Randomly sample, with replacement, 5000 probabilistic boundary delineations from both aerial images, overlay each sampled boundary to create polygons of erosion and deposition, and repeat using different A_{max} and A_{min} overlays (Figure 1 step 6). The distribution of areal changes represents the combined uncertainty in co-registration, digitization, and interpretation. A_{max} and A_{min} overlays include:
    a. Minimum active channel boundary in both images ($A_{Min(t1)}$&$A_{Min(t2)}$); where the subscripts *t1* and *t2* denote the earlier and later images, respectively (Figure 1 step 7a).
    b. Maximum active channel boundary in both images ($A_{Max(t1)}$&$A_{Max(t2)}$; Figure 1 step 7b).

c. Minimum active channel boundary in the earlier image and maximum active channel boundary in the later image ($A_{Min(t1)}$&$A_{Max(t2)}$; Figure 1 step 7c).

d. Maximum active channel boundary in the earlier image and minimum active channel boundary in the later image ($A_{Max(t1)}$&$A_{Min(t2)}$; Figure 1 step 7d).

References:

Gilvear D, Bryant R. 2003. Analysis of aerial photography and other remotely sensed data. In Tools in Fluvial Geomorphology , Kondolf MG and Piegay H (eds). Wiley: Chichester, U.K.; 135–170.

Hughes ML, McDowell PF, Marcus WA. 2006. Accuracy assessment of georectified aerial photographs: implications for measuring lateral channel movement in a GIS. Geomorphology **74** : 1–16. DOI: 10.1016/j.geomorph.2005.07.001

Mount NJ, Louis J, Teeuw RM, Zukowskyj PM, Stott T. 2003. Estimation of error in bankfull width comparisons from temporally sequenced raw and corrected aerial photographs. Geomorphology **56** : 65–77. DOI: 10.1016/S0169-555X(03)00046-1